



www.sciencemag.org/cgi/content/full/science.aad2085/DC1

## Supplementary Materials for

### **Molecular architecture of the human U4/U6.U5 tri-snRNP**

Dmitry E. Agafonov, Berthold Kastner, Olexandr Dybkov, Romina V. Hofele,  
Wen-Ti Liu, Henning Urlaub,\* Reinhard Lührmann,\* Holger Stark\*

\*Corresponding author. E-mail: reinhard.luehrmann@mpi-bpc.mpg.de (R.L.); hstark1@gwdg.de (H.S.);  
henning.urlaub@mpibpc.mpg.de (H.U.)

Published 18 February 2016 on *Science* First Release  
DOI: 10.1126/science.aad2085

#### **This PDF file includes:**

Materials and Methods

Figs. S1 to S16

Table S1

Captions for table S2 and movie S1

References

#### **Other supplementary material for this manuscript includes the following:**

Table S2 (Excel format)

Movie S1

# Supplementary online material

## Materials and Methods

### Purification of human U4/U6.U5 tri-snRNP

The nuclear extract for tri-snRNP purification was prepared essentially as described by Dignam *et al.* (1983) (37) with the following modifications. In brief, the nuclei pellet was resuspended in buffer containing 20 mM HEPES pH 7.9, 250 mM KCl, 8.5 mM MgCl<sub>2</sub>, 0.2 mM EDTA and 20% sucrose. The nuclei were lysed with 20 strokes of a Dounce homogenizer at 4 °C. The lysate was stirred for 40 min at 4 °C, followed by centrifugation in an SS34 rotor at 16,000 rpm for 30 min. The supernatant was additionally cleared by two consecutive centrifugations in an F14-6x250y rotor at 4 °C for 30 min at 13,000 and 14,000 rpm. 320 ml of the resulting supernatant was loaded onto a 17–30% sucrose gradient containing 20 mM HEPES pH 7.9, 150 mM KCl, 5 mM MgCl<sub>2</sub>, 0.1 mM EDTA in a Ti-15 zonal rotor (Beckmann Coulter) and centrifuged for 20 h at 4 °C. After gradient fractionation the U4, U5 and U6 snRNAs were detected by SYBR Gold (Invitrogen) staining of gradient fractions separated on a NuPAGE 4–12% Midi Gel (Invitrogen). Fractions containing tri-snRNPs were loaded onto an H20 column with bound m<sub>3</sub>G-cap antibody in the presence of approximately 15% sucrose from the gradient. Subsequent affinity chromatography was performed as described previously (12) in a buffer containing 20 mM HEPES pH 7.9, 150 mM KCl, 5 mM MgCl<sub>2</sub>, 0.1 mM EDTA and 15% sucrose. Eluted particles were loaded onto a 20%–50% sucrose gradient containing 20 mM HEPES pH 7.9, 100 mM KCl, 5 mM MgCl<sub>2</sub> and 0.1 mM EDTA. For mild fixation of particles for cryo-EM, the gradient also contained 0%–0.26% glutaraldehyde and 1 mM–0 mM p-maleimidophenyl isocyanate (PMPI, Pierce) from top to bottom. For biochemical controls the same gradient without glutaraldehyde and without PMPI was used. Centrifugation was performed at 29,000 rpm in a Surespin 630 rotor (Sorvall) for 40 h at 4 °C. Gradients were fractionated from the bottom. Aliquots of fractions were removed immediately and analyzed by a Bradford protein assay, and the remaining material in each fraction was quenched with 100 mM aspartate. The RNA and protein compositions of purified particles from non-fixed gradients were visualized after

separation on a NuPAGE 4–12% Midi Gel by staining with SYBR Gold (RNA) and with Coomassie blue (protein). Proteins were also analyzed on 2D gels as described previously (38).

### **Crosslinking of tri-snRNPs and crosslink identification by mass spectrometry**

Purified tri-snRNPs were cross-linked with 150  $\mu$ M BS3 and purified further by centrifugation in a 20-50% sucrose gradient. Approximately 40  $\mu$ g tri-snRNP pelleted by ultracentrifugation from the glycerol gradient fractions corresponding to 25S were analyzed essentially as described before (39), with the following modifications: precipitated material was dissolved in 4M Urea/50mM ammonium bicarbonate, reduced with DTT, alkylated with iodoacetamide, diluted to 1M Urea and digested with trypsin (1:20 w:w). Peptides were reverse-phase extracted and fractionated by gel filtration on Superdex Peptide PC3.2/30 column (GE HealthCare). 50  $\mu$ l fractions corresponding to elution volume of 1.2-1.8 ml were analyzed on Orbitrap Fusion Tribrid (dataset 1), Q Exactive HF (dataset 2) or Q Exactive (dataset 3) mass spectrometers (Thermo Scientific). Protein-protein crosslinks were identified by pLink1.22 search engine and filtered at FDR 1% ([pfind.ict.ac.cn/software/pLink](http://pfind.ict.ac.cn/software/pLink)) according to the recommendations of the developers (40). For simplicity, the crosslink Score is represented as a negative value of the common logarithm of the original pLink Score, that is  $\text{Score} = -\log_{10}(\text{pLink Score})$ . Dataset 1 was not filtered further, while the filtering criteria of  $\text{Score}_{\max} \geq 1$  or  $\text{Score}_{\max} \geq 3$  were applied for the datasets 2 and 3, respectively (table S2). 169 BS3-crosslinks were identified between the known structured tri-snRNP protein domains. For model building, a maximum distance of 3 nm between the C $\alpha$ -atoms of the crosslinked lysines was allowed. The actual distribution of C $\alpha$ - C $\alpha$  distances between crosslinked residues that can be mapped in the model of the tri-snRNP is shown in fig. S16.

### **Electron Microscopy**

Purified tri-snRNPs were allowed to adsorb on a thin film of carbon for 10 min, transferred onto a cryo-EM grid (Quantifoil 3.5/1 1 $\mu$ m, Jena) and then prepared under controlled environmental conditions of 4  $^{\circ}$ C and 100% humidity in a vitrification device (Vitrobot Mark IV, FEI Company, Eindhoven). Images were recorded in spot-scanning

mode ( $2 \times 2$  image frames per  $3.5 \mu\text{m}$  hole in the Quantifoil carbon film) on a Falcon II direct detector under liquid-nitrogen conditions with a Titan Krios electron microscope (FEI, Eindhoven) equipped with a XFEG electron source and a  $C_s$  corrector (CEOS, Heidelberg) using 300 kV acceleration voltage. An electron dose of  $\sim 30$  electrons per  $\text{\AA}^2$ ,  $-0.7$  to  $-2.5 \mu\text{m}$  defocus and a nominal magnification of  $74,000\times$  were used, resulting in a final pixel size of  $\sim 2 \text{\AA}$ . 1,150,811 particle images were initially extracted in a fully automated manner using template-independent custom-made software (CowPicker, B. Busche and H.S., unpublished data). The extracted particle images were corrected locally for the contrast-transfer function by classification and averaging and selected according to quality of power spectra (41). Initial sorting of images was performed based on CTF parameters. Only images showing Thon rings better than 7 Angstrom were used for further processing. Additional sorting was performed applying two rounds of multivariate statistics, first without alignment and subsequently after one round of image alignment. This resulted in a total number of 636,460 particle images that were used for further processing. 3D classification in RELION 1.2 (42) was used to obtain 190,939 intact tri-snRNP particles using a previously published 3D structure as a reference (EMD-1729). A second round of 3D classification yielded the 141,109 particle images that were used for the final refinement that resulted in a  $7 \text{\AA}$  resolution structure (using the ‘gold-standard procedure’ in RELION 1.2) by applying a mask that covers the entire tri-snRNP. The structure was used for manual model building in UCSF Chimera 1.10.1 (43).

### **Preparation of Figures**

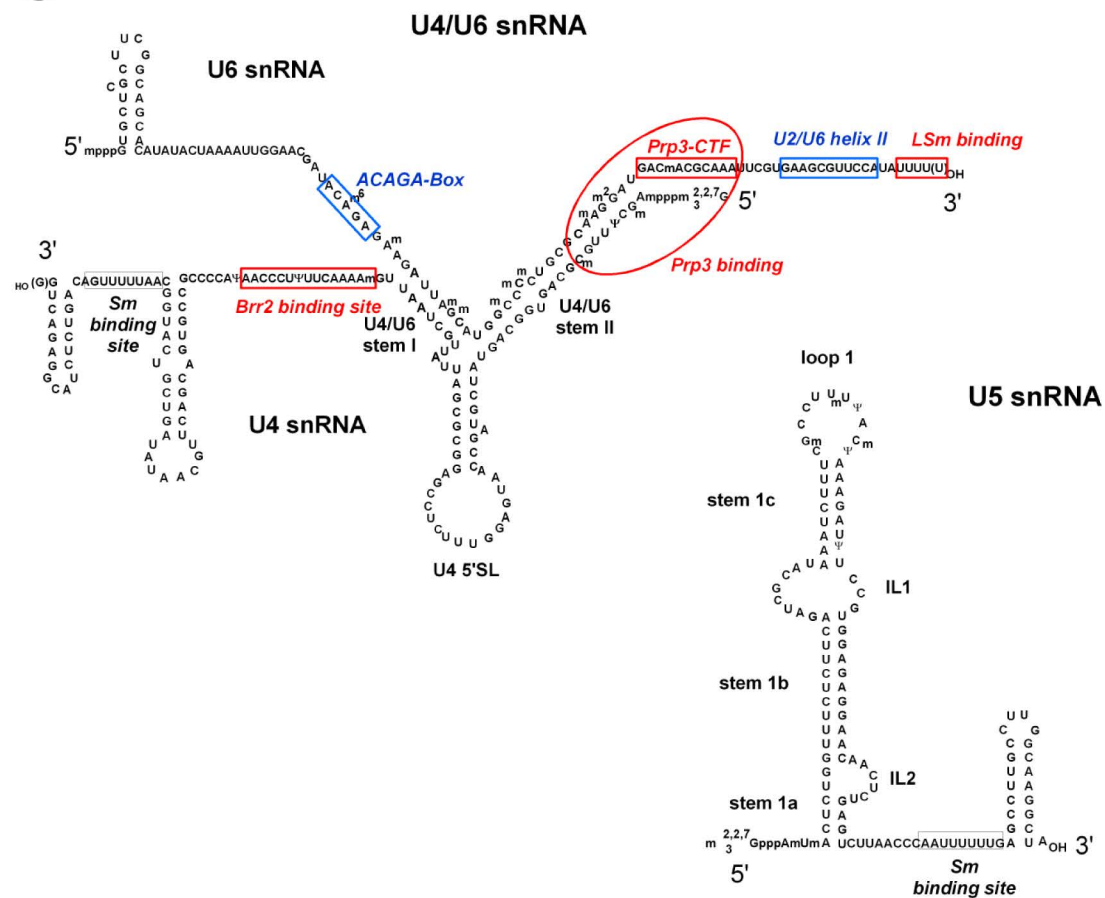
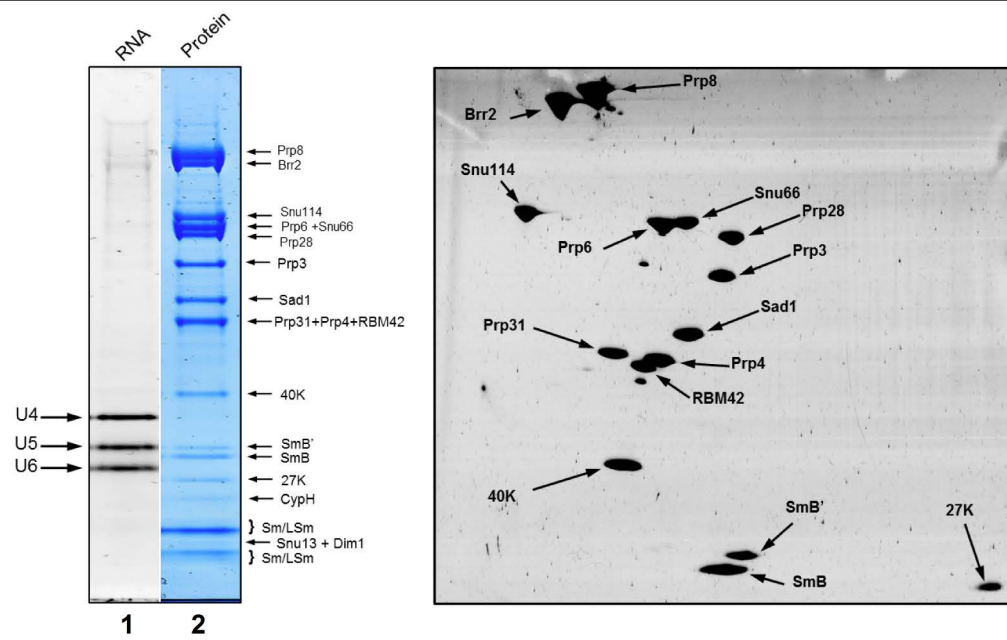
Maps were visualized and movie and figures generated using UCSF Chimera (43), except figures S6, S7C, D and S15 which were generated by PyMOL Molecular Graphics System.

## Supplementary Figure Legends

**Figure S1. Protein and RNA composition of human U4/U6.U5 tri-snRNPs used for cryo-EM.** (A) Proteins present in human tri-snRNPs and their molecular mass. The yeast (*S. cerevisiae*) nomenclature was used for all human tri-snRNP proteins also present in *S. cerevisiae*. The U5-40K, cyclophilin H (CypH), 27K and RBM42 proteins do not have counterparts in *S. cerevisiae*. Alternative names for the human tri-snRNP proteins are also listed. (B) RNA and protein composition of purified human HeLa U4/U6.U5 tri-snRNPs. Left panel: SDS-polyacrylamide gel stained with SYBR Gold (lane 1) or Coomassie (lane 2) showing the snRNA and protein composition, respectively, of purified tri-snRNPs. Proteins were identified by mass spectrometry. Right panel: RuBPS-stained, two-dimensional gel of tri-snRNP proteins separated according to (38). Proteins with a molecular weight less than ca. 25 kDa have run out of the gel. (C) RNA sequences and secondary structures of human U5 snRNA and base-paired U4 and U6 snRNAs. Red boxes indicate regions of the snRNAs that interact with the LSm2–8 and Prp3 proteins in the isolated tri-snRNP, or with the Brr2 RNA helicase in the course of U4/U6 snRNA unwinding during activation of the spliceosomal B complex. Blue boxes show the regions of U6 snRNA (its 3' end) that base pair with the 5' end of U2 snRNA to form the U2/U6 helix II, and with the 5' splice site (ACAGA box), during B complex formation.

**A**

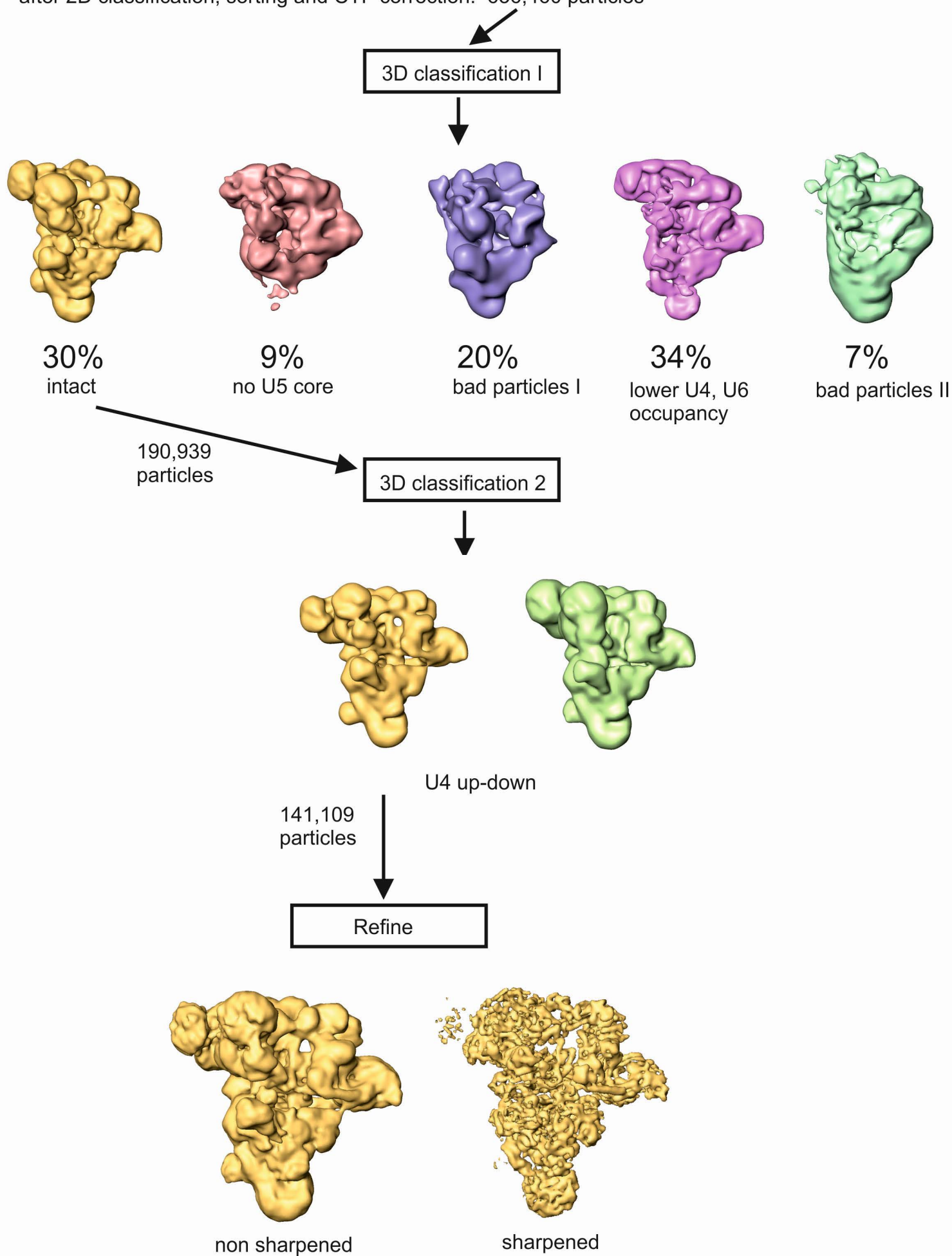
Name		Size	Name		Size
used	other	kDa	used	other	kDa
<i>U5 snRNP specific proteins</i>					
<b>Prp8</b>	U5-220K	273.6	<b>Prp3</b>	U4/U6-90K PRPF3	77.5
<b>Brr2</b>	U5-200K SNRNP200	244.5	<b>Prp31</b>	U4/U6-61K NY-BR-99 PRPF31	55.5
<b>Snu114</b>	U5-116K EFTUD2	109.4	<b>Snu13</b>	U4/U6-15.5K NHP2L1	14.2
<b>40K</b>	SNRNP40	39.3	<b>Prp4</b>	U4/U6-60K Q5T1M7 PRPF4	58.4
<b>Dim1</b>	U5-15K Dib1 TXNL4A	16.8	<b>CypH</b>	U4/U6-20K PPlaseH PPIH	19.2
<b>Prp28</b>	U5-100k DDX23	95.6	<i>tri-snRNP specific proteins</i>		
<b>Prp6</b>	U5-102K ANT-1 PRPF6	106.9	<b>Sad1</b>	U5.U4/U6-65K USP39 SNUT2	65.4
Sm proteins, U4 and U5 RNA associated					
<b>Sm B/B', D3, D2, D1, E, F, G</b>		9 - 24	<b>Snu66</b>	U5.U4/U6-110K Sart1 SNUT1	90.3
LSm proteins, U6 RNA associated					
<b>LSm 2, 3, 4, 5, 6, 7, 8</b>		9 - 15	<b>27K</b>	U5.U4/U6-27K SNRNP27 SNUT3	18.8
			<b>RBM42</b>		50.4

**C****B**

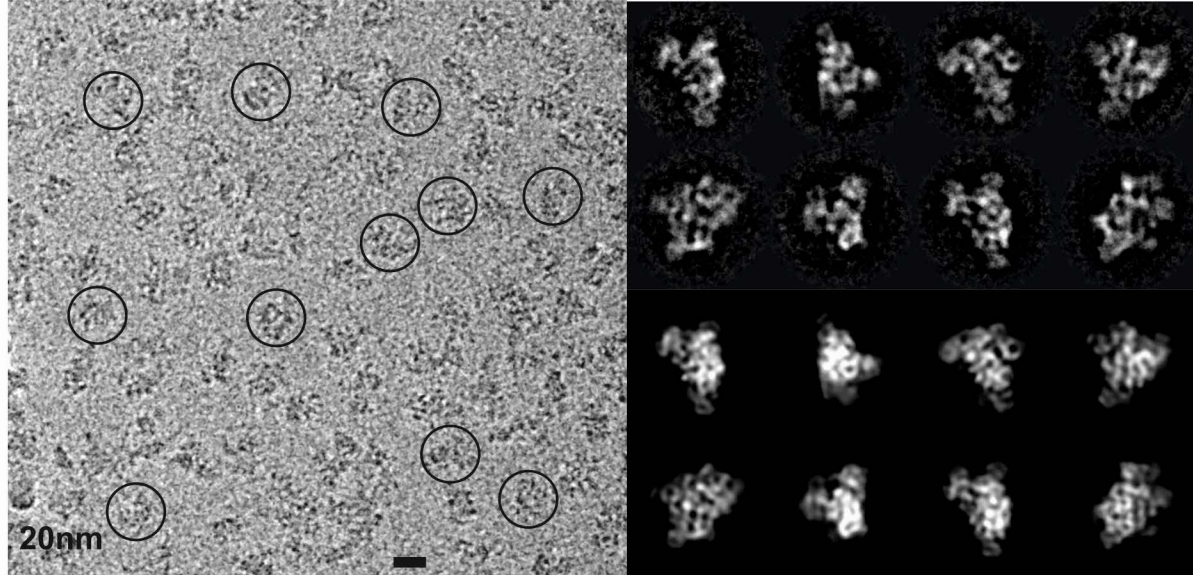
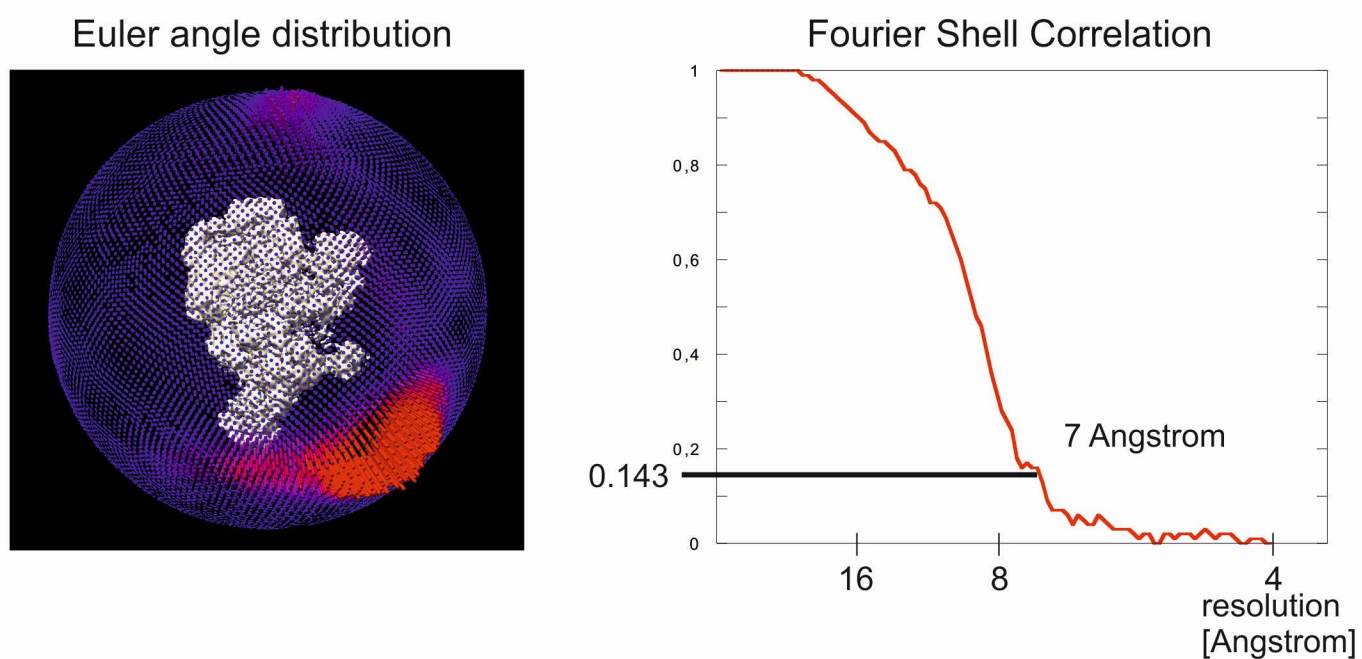
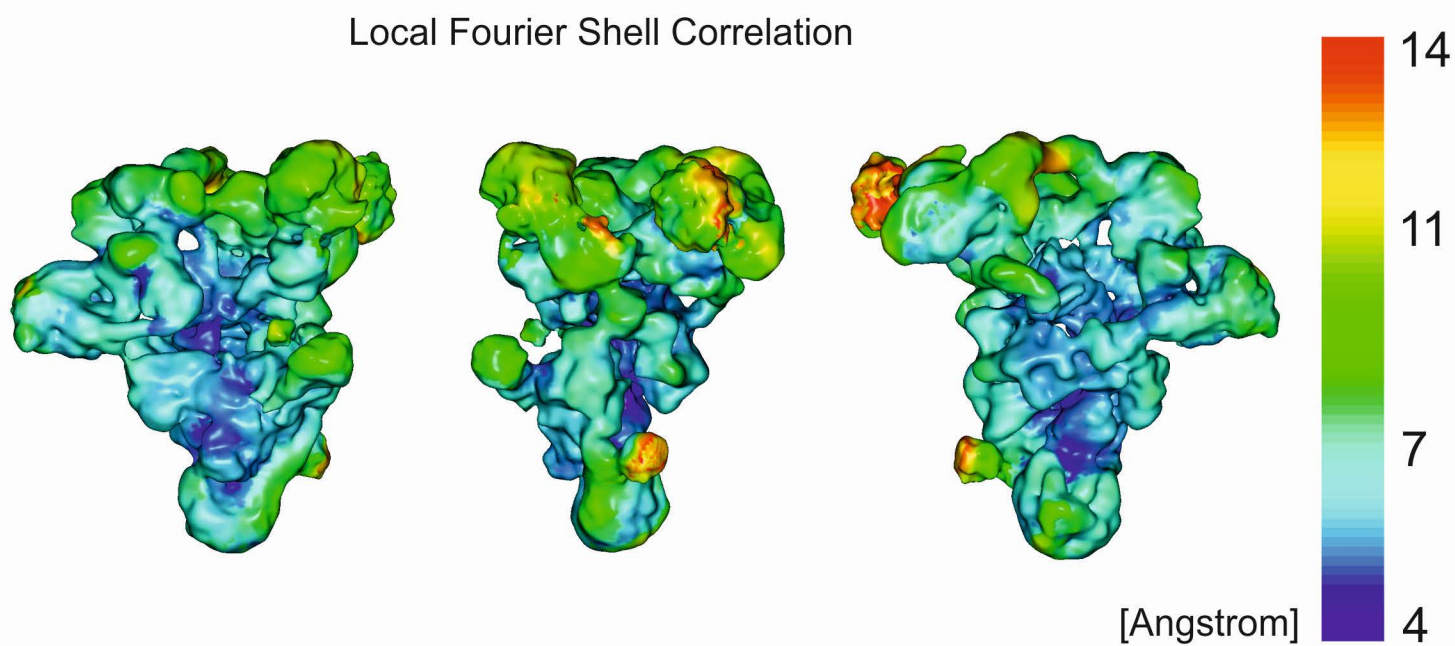
## **Figure S2. Computational Sorting**

4812 micrographs were recorded from which 1,150,811 particle images were selected by a newly developed particle picking software that does not require reference images for particle selection. After 2D classification, sorting of particles and CTF correction, 636,460 particles were used for structure calculations. Our previously determined low-resolution structure of the tri-snRNP was used as a reference to obtain the initial 3D structure. 3D classification was performed in RELION. Roughly 30% of the particles revealed intact tri-snRNPs. Other populations revealed mainly tri-snRNPs that had lost one or more of the Sm cores or other proteins. 190,939 particles were analyzed in a second classification step and revealed tri-snRNPs that mainly differed in the conformation of the U4 Sm core which seems to be flexible. A population of 141,109 particles was used for the final refinement to obtain the 7 Å 3D structure. Shown is the structure prior to sharpening and the sharpened map that was calculated using a B factor of 250.

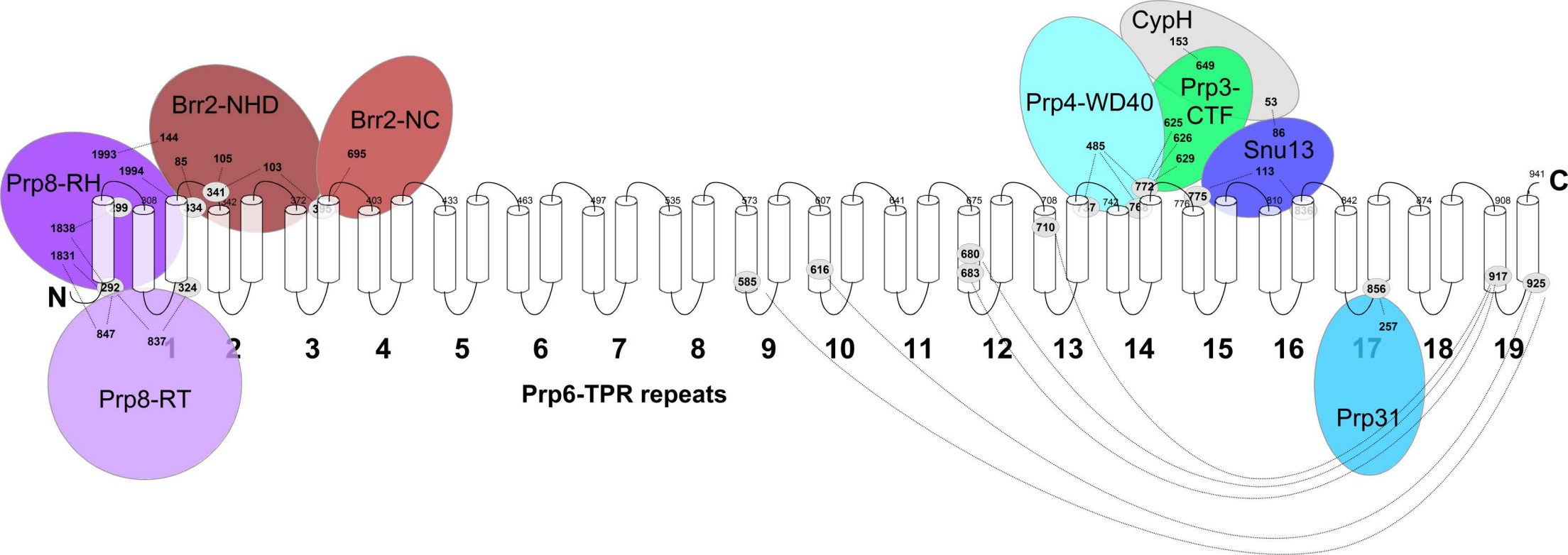
4,812 micrographs  
picked particles: 1,150,811  
after 2D classification, sorting and CTF correction: 636,460 particles



**Figure S3. Cryo-EM and image processing of the human tri-snRNP.** (A) Raw images of vitrified tri-snRNPs imaged with a Titan Krios electron microscope at 74,000x magnification on a Falcon II direct detector. Some tri-snRNPs are encircled. The panels on the right show 2D class averages obtained after alignment and classification (upper 2 rows) and their corresponding reprojections calculated from the 3D structure (lower 2 rows). (B) Left: Euler angle distribution obtained for the final 3D reconstruction. Tri-snRNP molecules exhibit a relatively strong preference to bind to carbon film. This is reflected by the red bars of the spherical histogram. However, the presence of almost all other possible views becomes obvious from the relatively uniform distribution as indicated by the blue bars. Right: Fourier-shell-correlation function of two independently refined half maps indicate a resolution of 7 Å using the 0.143 threshold. (C) Local resolution plot obtained from calculating local Fourier-shell correlations using a kernel of 15x15x15 voxel over the entire 3D volume. Three different views of the tri-snRNP are depicted which are rotated along the vertical axis. The tri-snRNP map is best defined in the center of the particle where the resolution exceeds the average resolution obtained for the entire reconstruction. The resolution drops below 10 Å in some areas of the map. The lower resolution in the U4/U6 part of the tri-snRNP (top region) can be explained by compositional and/or conformational heterogeneity.

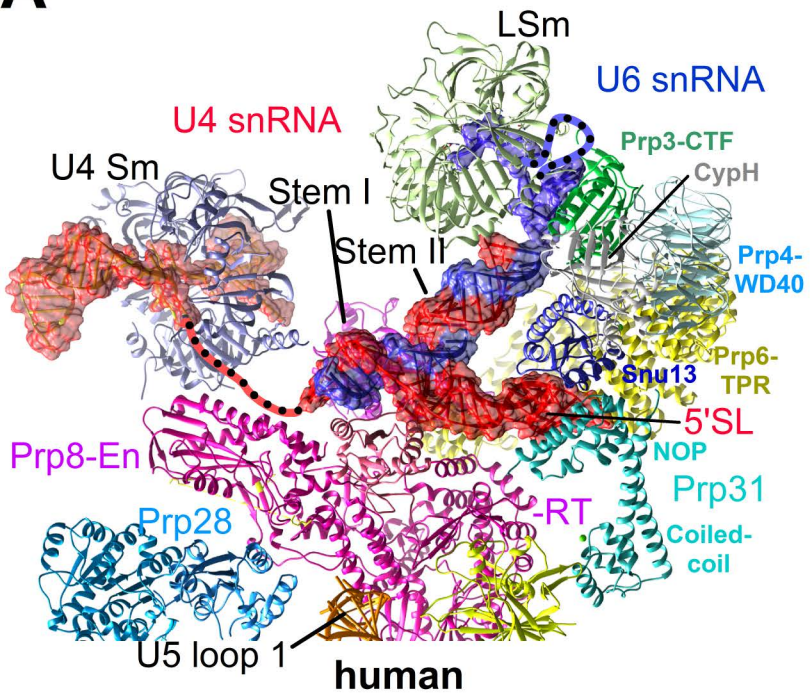
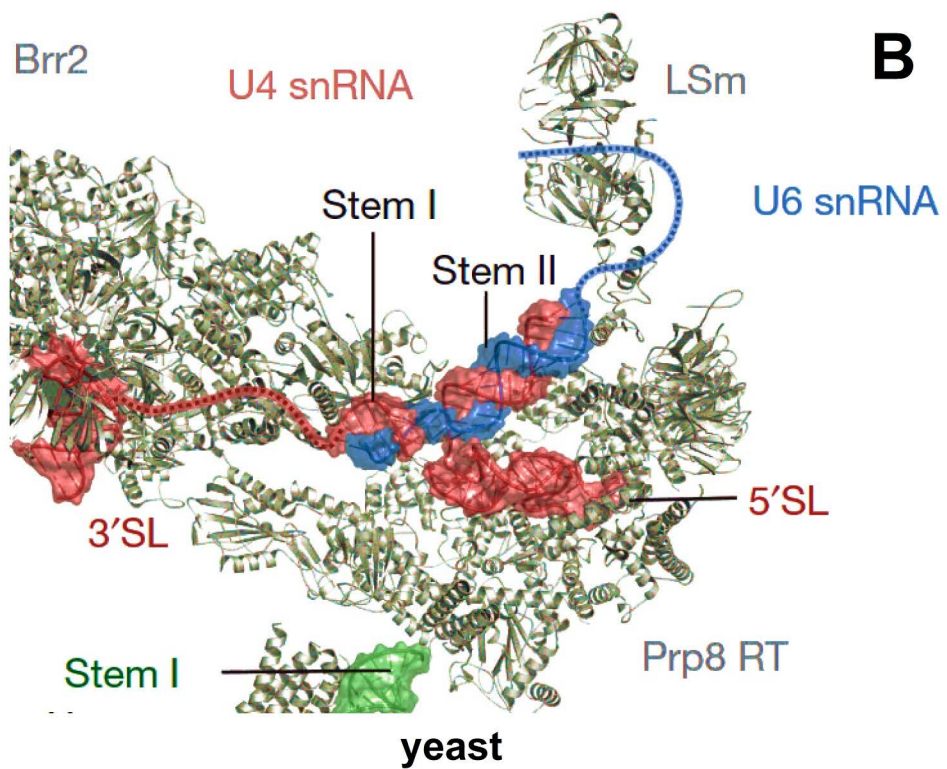
**A****B****C**

**Figure S4. Crosslinking of the C-terminal TPR repeats of Prp6 to U4/U6 proteins and its N-terminal TPR repeats to U5 proteins Prp8 and Brr2.**  $\alpha$ -Helical regions of Prp6 TPR repeats 1–19 are indicated by cylinders. The numbers of crosslinked lysine residues (connected by stippled lines) correspond to their positions in the respective protein sequences. Intramolecular crosslinks between TPR18-19 and TPRs 9-13 of Prp6 are also indicated by stippled lines. Brr2-NHD, N-terminal helical domain of Brr2; Brr2-NC, N-terminal helicase cassette of Brr2 (see also Figs. 2 and 4).

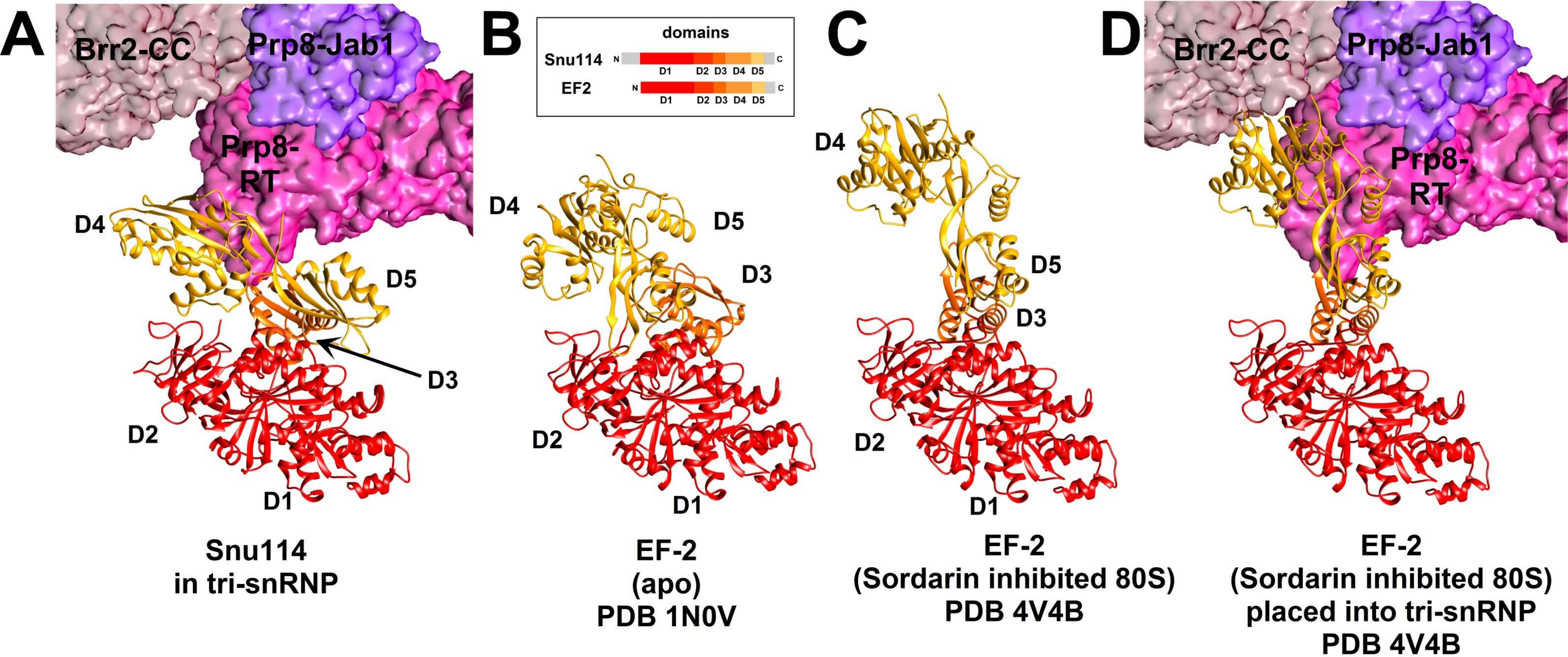


**Figure S5. Similarities and differences in the architecture of the U4/U6 snRNP in the human and yeast tri-snRNP models.**

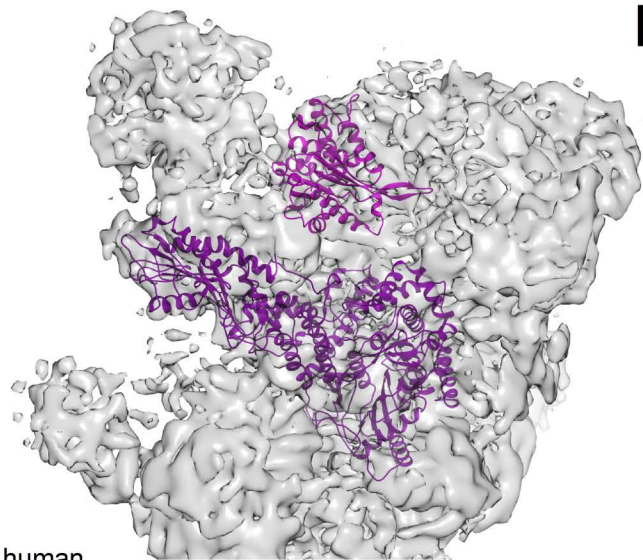
Structures of the U4/U6 snRNA and proteins in corresponding views of the human (A) and yeast (B) tri-snRNP model (9). The geometry of the base-paired U4/U6 regions of the three-way junction is essentially the same in both models. In the human tri-snRNP, the position of the LSm ring is closer to the region between the U4/U6 stem II and the single-stranded 3' end of the U6 snRNA than in the yeast tri-snRNP. In the human tri-snRNP, the ferredoxin-like domain of Prp3-CTF faces the LSm structure in such a way that the single-stranded 3'-terminal region of the U6 snRNA can be continued in the direction of the LSm doughnut (dotted purple line, panel A). The U4 Sm core structure is also positioned differently in the two tri-snRNP models (see superposition of the human and yeast tri-snRNP models in fig. S12) and the architecture of the Prp31 protein also differs. That is, the crystal structure of the arc-like form of Prp31's coiled-coil and Nop domain fits perfectly into a similarly shaped density element in the human tri-snRNP that is bent downwards at the periphery of the tri-snRNP contacting the Sad1 protein (Figs. 2A and 5). In contrast, in the yeast tri-snRNP model, the coiled-coil domain of Prp31 is rotated by ca. 60° with respect to the Nop domain (9).

**A****B**

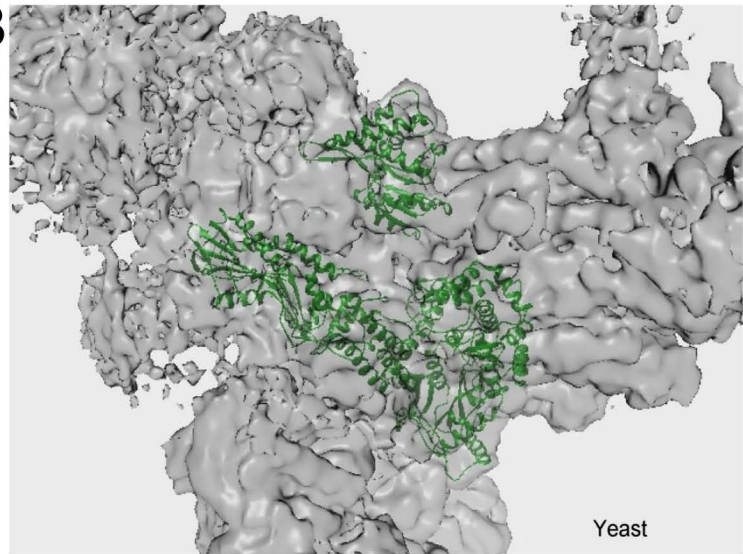
**Figure S6. Snu114 has a structure in the human tri-snRNP similar to the compact form of the elongation factor EF-2.** (A) Structural organization of Snu114 in the human tri-snRNP; the positions of the Prp8 RT and Brr2 CC domains that are closest to Snu114's D3 to D5 domains in the tri-snRNP model are also shown. With the exception of its N-terminal 115-residue domain, the 116-kDa protein Snu114 is highly homologous to the ribosomal elongation factor EF-2/EF-G (see inset). The compact form (B) of crystallized EF-2 (16) and its extended form (C) as observed in the 80S ribosome post-translocation state (35). All structures are aligned via domains D1 and D2. A comparison of the structure of Snu114 with those of EF-2 reveals significant similarity with the compact EF-2 form. (D) The elongated form of EF-2 (35) modelled into the tri-snRNP structure, whereby domains D1 and D2 are aligned to the position of Snu114's D1 and D2 in the tri-snRNP. If during the catalytic activation of the spliceosome Snu114 would undergo a structural change in the direction of the extended form of EF-2, then domains D4 and D5 would lie at the interface between Prp8-RT and Brr2-CC, and would clash with Brr2-CC. Thus, such a conformational change in Snu114 would only be possible if it were part of a concerted structural change in the spliceosome, including movement of Brr2 toward U4/U6 RNAs (see also main text and fig. S14).



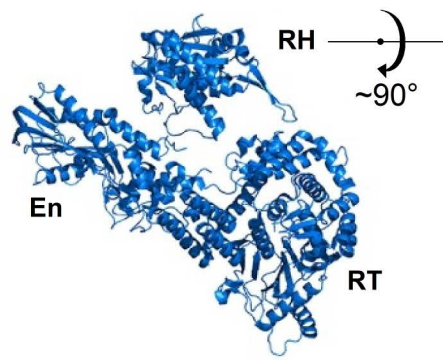
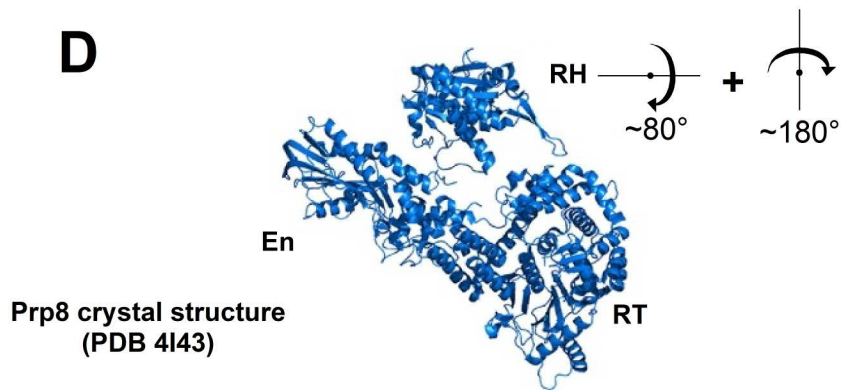
**Figure S7. Differences in the architecture of the Prp8 RH domain in the cryo EM structures of human and yeast tri-snRNPs.** The structures of the Prp8 RT/En and Prp8 RH domains are shown in corresponding views of the human (**A**) and yeast (**B**) tri-snRNP model (9). (**C** and **D**) Structure of the yeast Prp8 RT/En and Prp8 RH domain as found in the crystallised complex with the Aar2 protein (44). The spatial organization of the Prp8 RT/En domain is almost identical in the two tri-snRNP structures. The positions of the RH domains relative to the axis of the respective Prp8 RT/En domains are also similar. However, the spatial orientation of the RH domain differs significantly between the two structures. In the human tri-snRNP structure, the RH domain is rotated by approximately 90° relative to its position in the crystal structure (A and C). In the yeast tri-snRNP, it must be rotated additionally by 180° about the central axis. Thus, in the human tri-snRNP the  $\beta$  hairpin of the RH domain points towards the RT domain, while in the yeast tri-snRNP it points in the opposite direction, i.e. towards the En domain of Prp8.

**A**

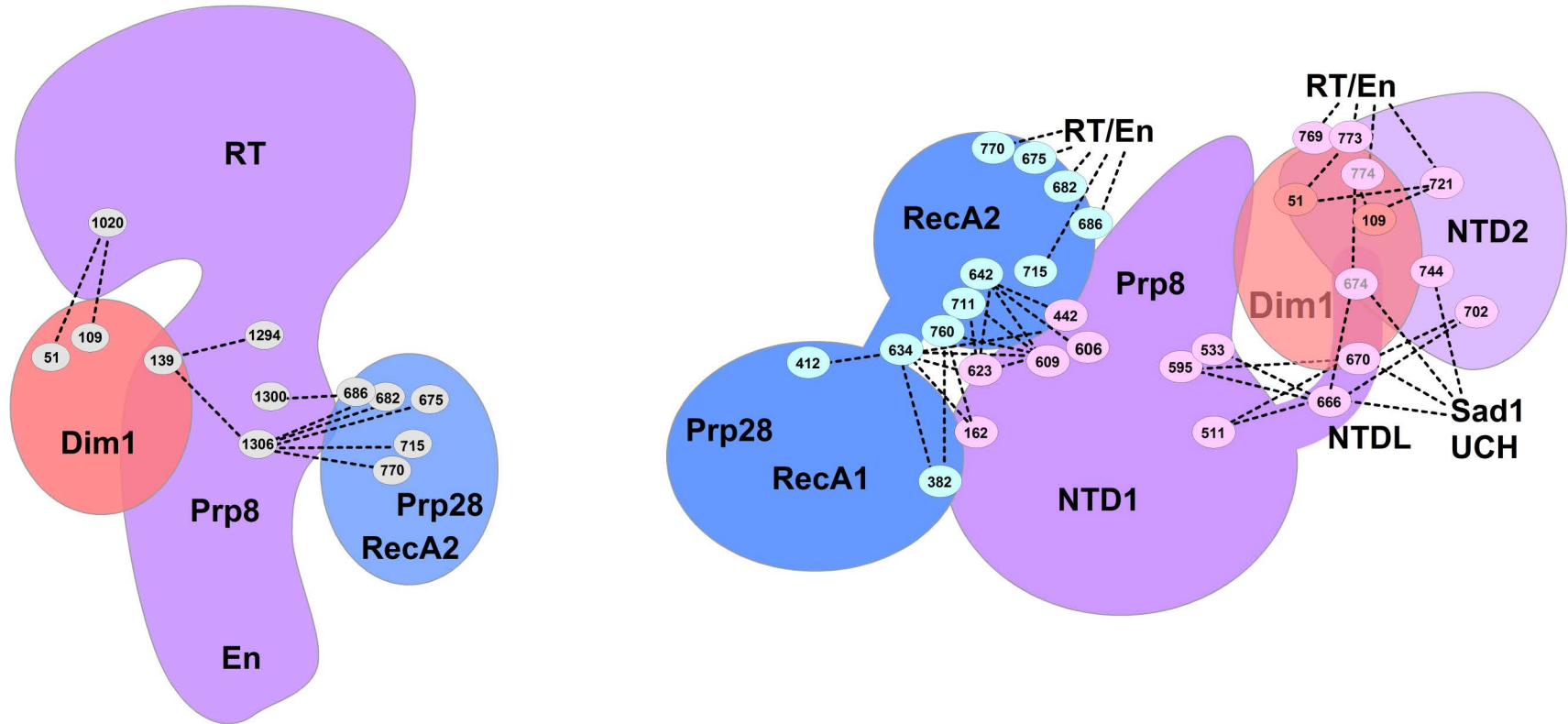
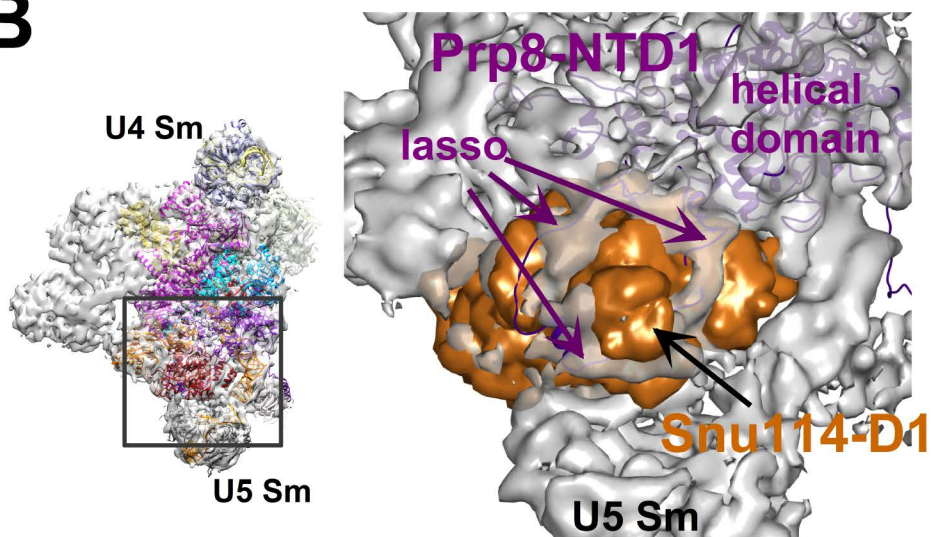
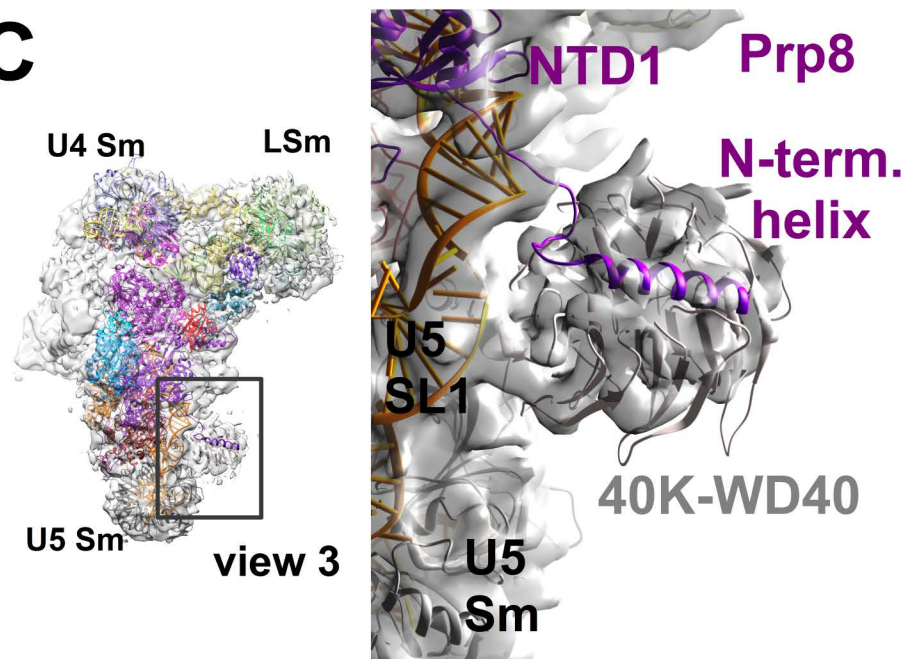
human

**B**

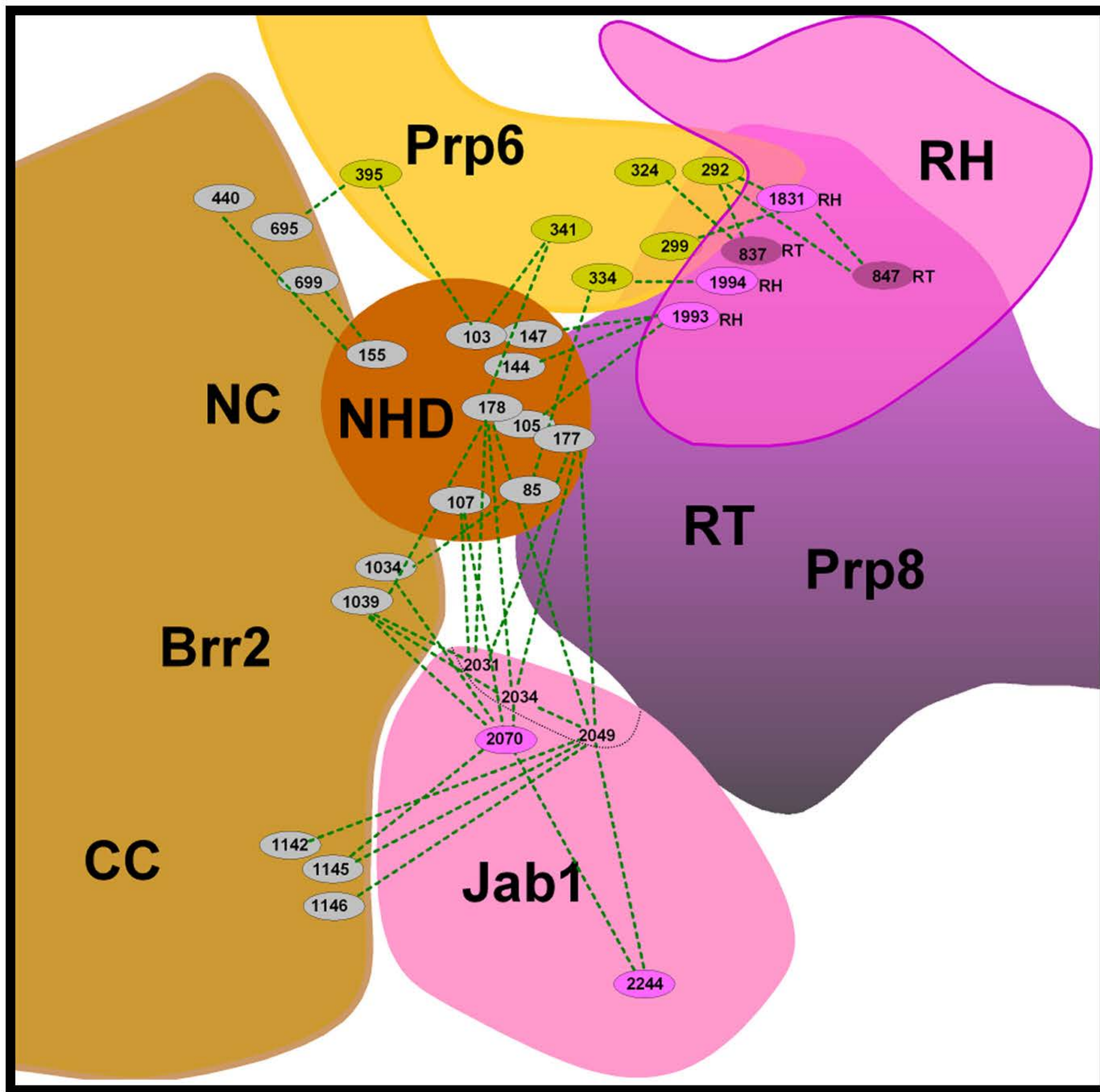
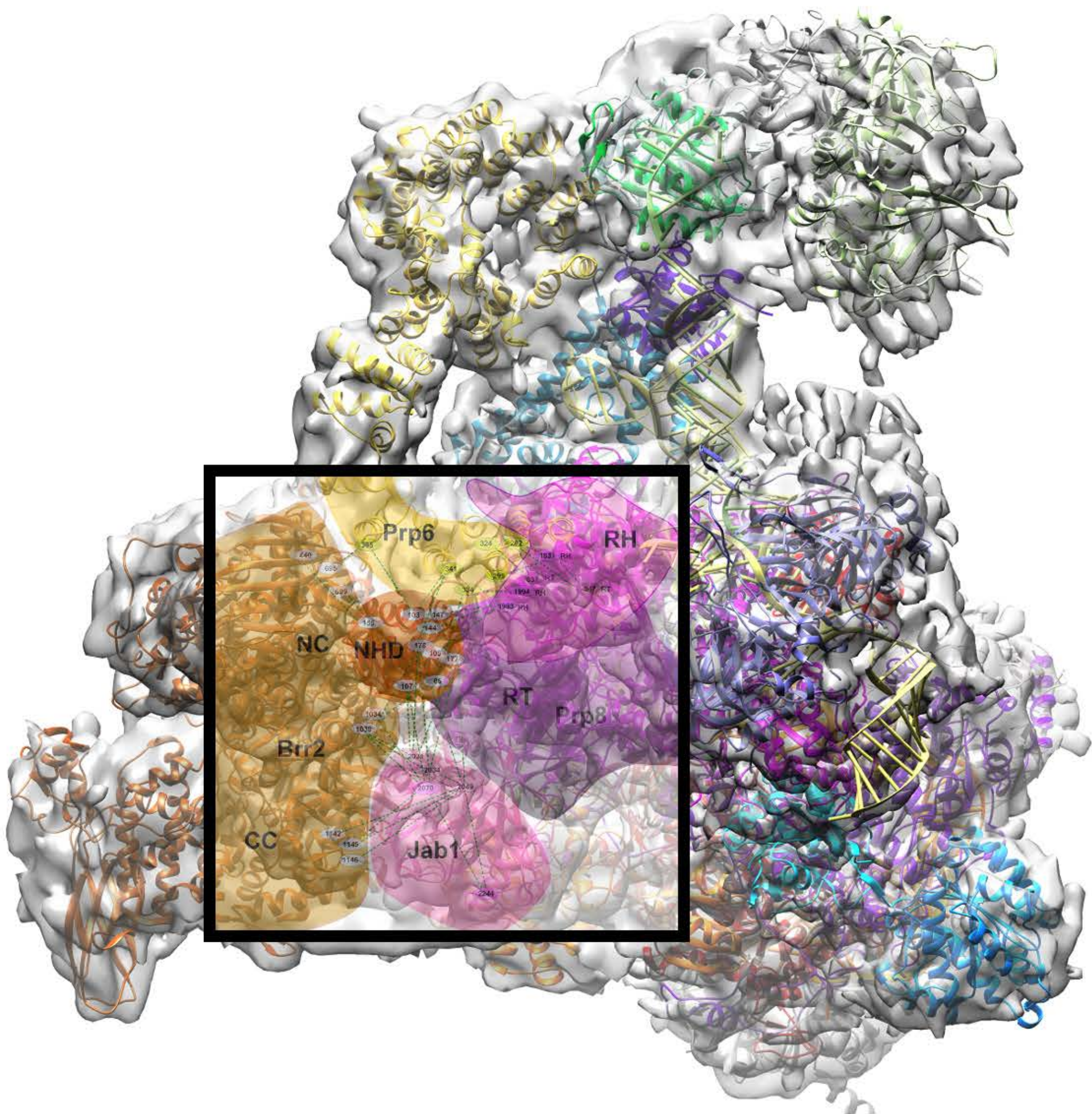
Yeast

**C****D**

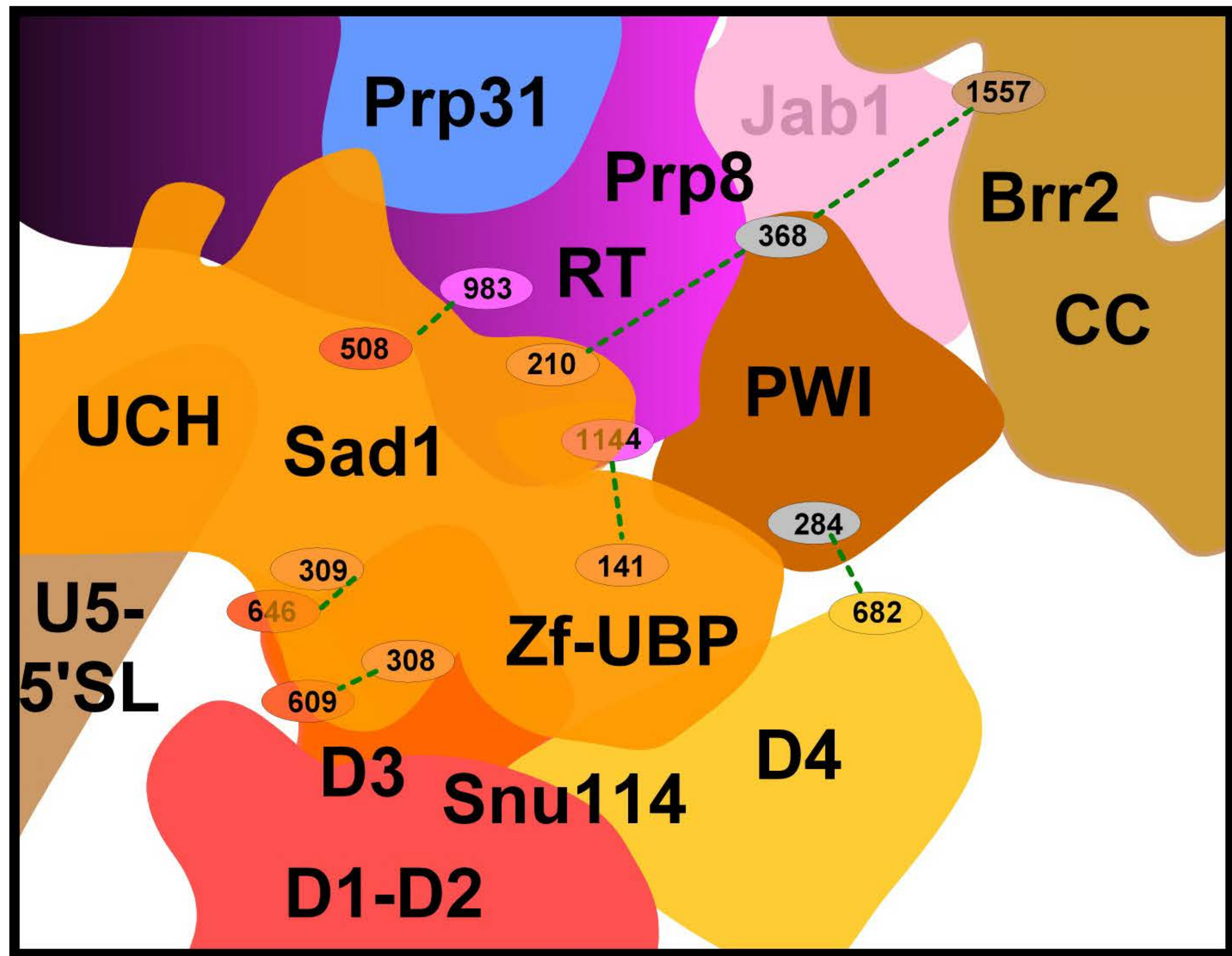
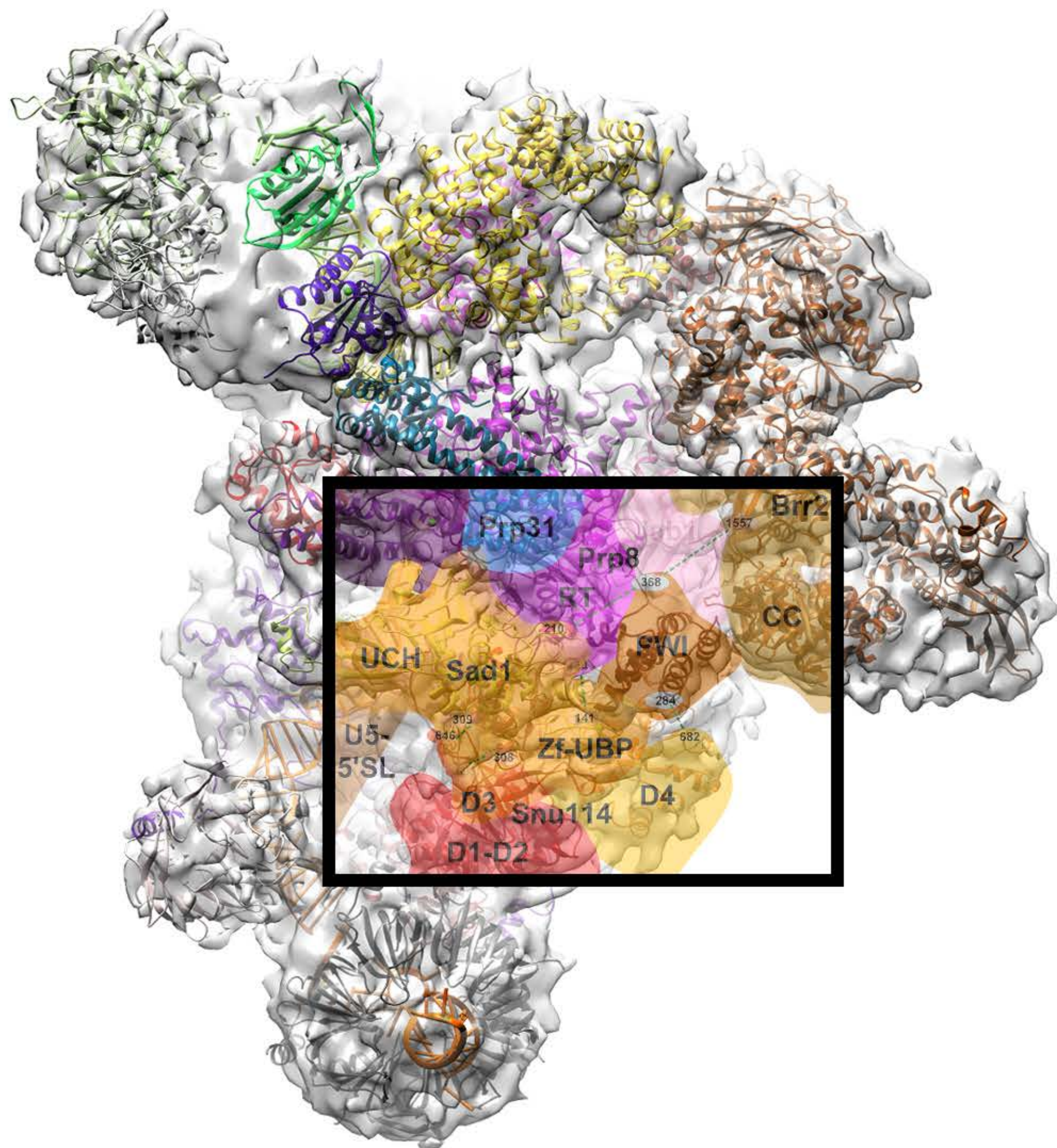
**Figure S8. Prp8 interactions and crosslinks with Prp28, Dim1, Snu114 and the U5-40K protein.** (A) Intermolecular crosslinks between Prp8's RT/En, NTD1, NTD2, and NTDL domains, and Dim1 and the RecA2 domain of Prp28. Numbers indicate positions of crosslinked lysine residues in the three proteins. (B) Left: View 1 of the human tri-snRNP. Right: expanded view of boxed region, with Snu114 colored in orange. Prp8's NTD1-lasso interacts with the D1 domain of Snu114 in the tri-snRNP in a similar manner as in the *S. pombe* spliceosome (10). The NTD1 lasso (in lilac) of the *S. pombe* spliceosome (10) fits as a rigid body into the ring-like density element (in grey) encircling part of the Snu114 D1 domain in the tri-snRNP model (shown in space filling mode). (C) Location of the WD40 domain of U5-40K. Left: View 3 of the human tri-snRNP. Right: Expanded view of boxed region. The 40K-WD40 domain fits into a peripheral knob-like density element at the bottom of the tri-snRNP, close to the internal loop 2 of U5 snRNA. There is a density element on top of the WD40 domain into which the N-terminal helix of Prp8's NTD1 fits well, consistent with protein-protein crosslinks between both protein domains in the tri-snRNP (table S1 and S2)

**A****B****C**

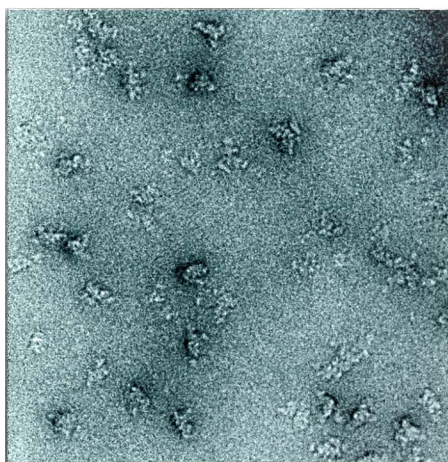
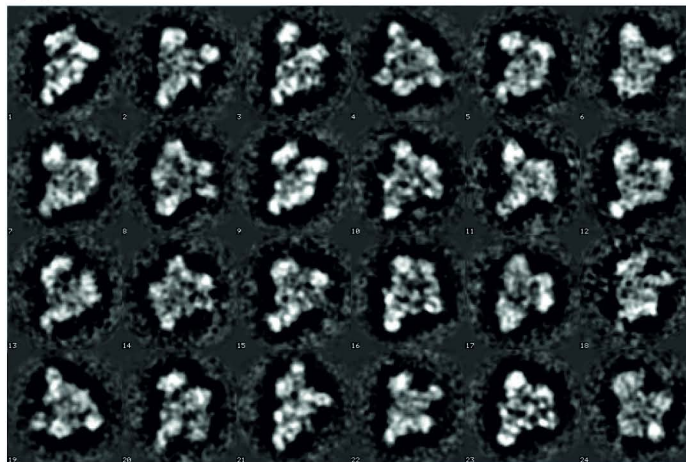
**Figure S9. Intermolecular crosslinks support the juxtaposition of Brr2 domains with Prp6's N-terminal TPR repeats and Prp8's RT, RH and Jab1 domains.** Left panel: View of the human tri-snRNP from the top. The frame highlights the spatial relationships between the density elements of the cryo-EM structure with (i) the fitted crystal structures of the Brr2-NC, Prp8-Jab1/Brr2-CC and Prp8 RH and RT domains and (ii) the fitted, modelled N-terminal TPRs of Prp6 and NHD of Brr2. Right: Intermolecular crosslinks between the protein domains are shown. Numbers indicate the positions of crosslinked lysine residues (connected by stippled lines) in each protein. Although projected onto the plane of the paper, the positions in space of the crosslinked lysines correspond to their positions in the 3D structures of their respective protein domains. The maximum observed length for any crosslink was 30 Å. An internal crosslink (2034–2049) and several crosslinks from these two positions to lysines 2070 and 2244 of the Jab1 domain were detected in the ~35-residue-long tract of Prp8, which lies immediately on the N-terminal side of the crystallised Jab1 domain of Prp8 (residues 2067–2305). We therefore placed this region (small area in pink Jab1 region indicated by a dotted line) next to Jab1 (see also table S1).



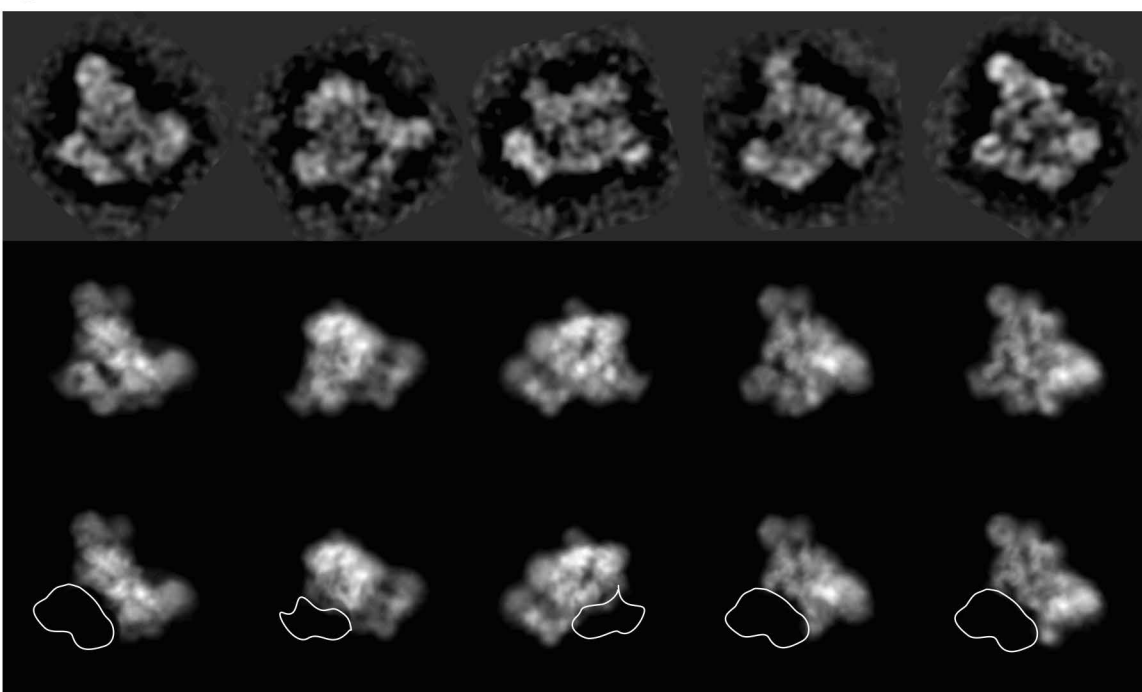
**Figure S10: Network of crosslinks between Brr2, Sad1, Snu114 and Prp8 RT domains.** Left: View 5 of the human tri-snRNP. The frame highlights the spatial relationships between the density elements of the cryo-EM structure with (i) the fitted crystal structures of Sad1, the Brr2-CC, Brr2-PWI, Prp8-Jab1 and Prp8 RH domains, and (ii) the fitted, modelled D1 to D4 domains of Snu114. Right: Intermolecular crosslinks between the protein domains shown. Numbers indicate the positions of crosslinked lysine residues (connected by stippled lines) in each protein. Although projected onto the plane of the paper, the positions in space of the crosslinked lysines correspond to their positions in the 3D structures of their respective protein domains.



**Figure S11. Brr2 is located in a similar position in native human tri-snRNPs not subjected to chemical crosslinking.** (A) Raw image of non-fixed human tri-snRNPs by negative stain electron microscopy. The purified complexes were stained with uranyl formate, air dried and imaged at RT in a Philips CM12 electron microscope. (B) 21.747 tri-snRNP particles were selected for image processing. Typical class averages are shown after several rounds of alignment and classification without using a 3D model as template. (C) Upper row: class averages from negatively-stained human tri-snRNP particles that were not crosslinked. Middle row: reprojections calculated from the cryo-EM 3D structure that was determined from a GraFix treated sample. Projection angles were assigned to class averages by projection matching using the cryo-EM 3D model without Brr2 density (see D) as an initial reference. Overall, the structural features match very well. Lower row: reprojections calculated from the cryo-EM map after removing the Brr2 density. The reprojections therefore show no density for Brr2 and the areas of the missing density are marked by the white lines. We therefore conclude that the position of Brr2 within the tri-snRNP is not affected by the use of chemical crosslinking. (D) Surface view of the cryo-EM reconstruction obtained from GraFix treated tri-snRNPs. The position of Brr2 is marked with a white line. (E) Low resolution reconstruction obtained from negatively-stained images from non-crosslinked tri-snRNPs. Density for Brr2 is clearly visible even at low resolution.

**A****B**

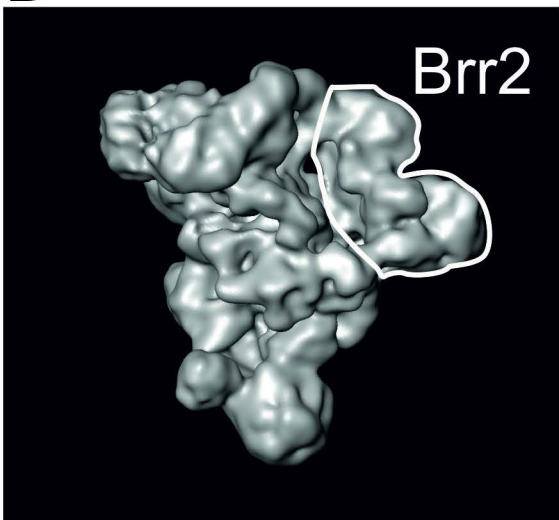
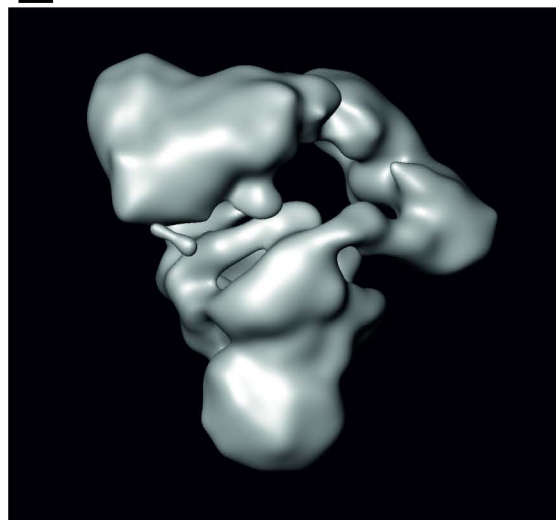
„non-fixed“  
class averages

**C**

„non-fixed“  
class averages

Corresponding  
projections

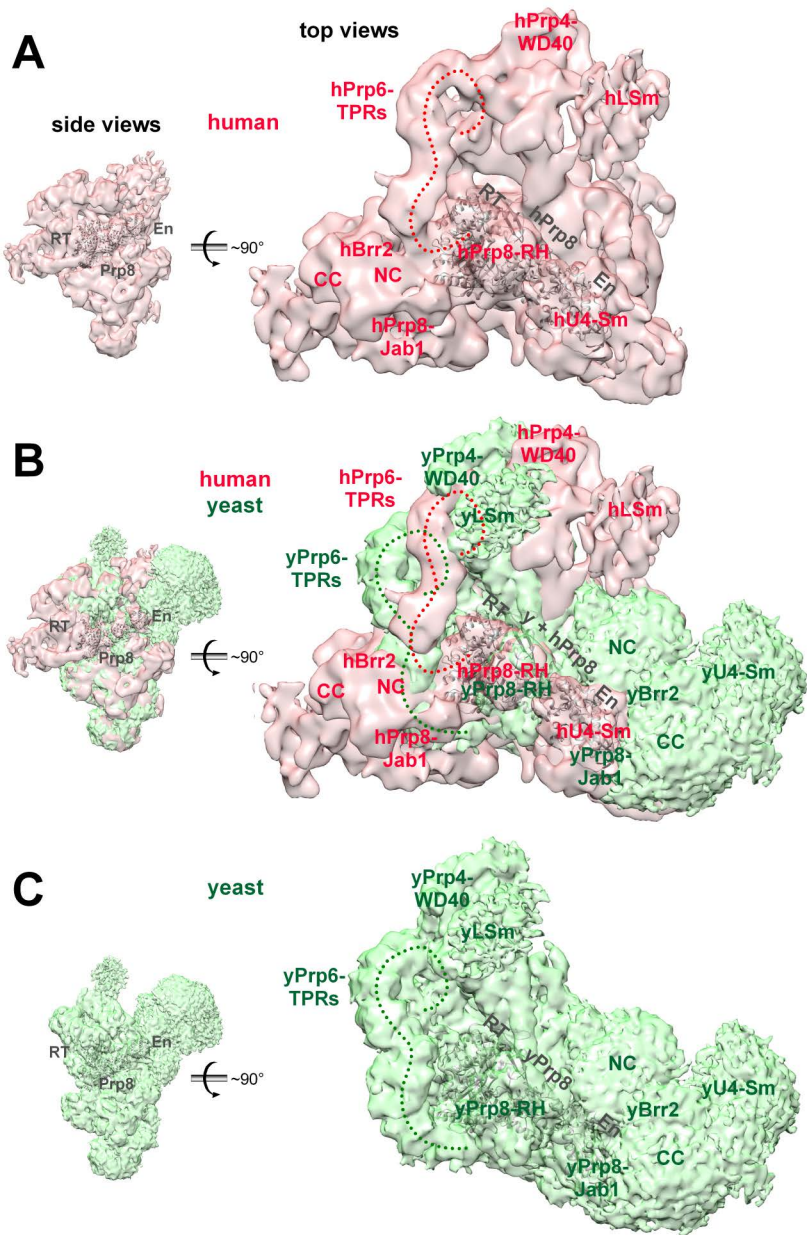
Rejections from delta-Brr2  
structure

**D****E**

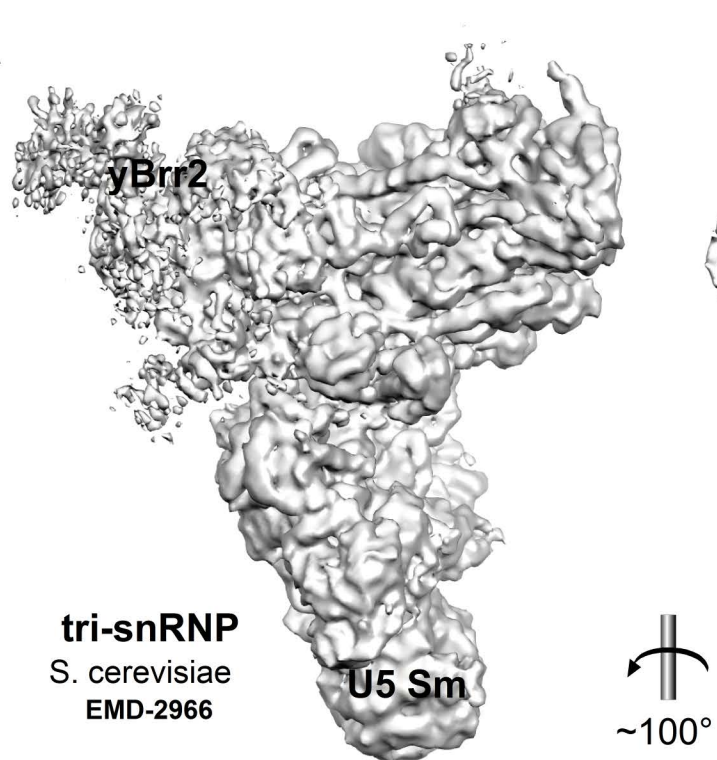
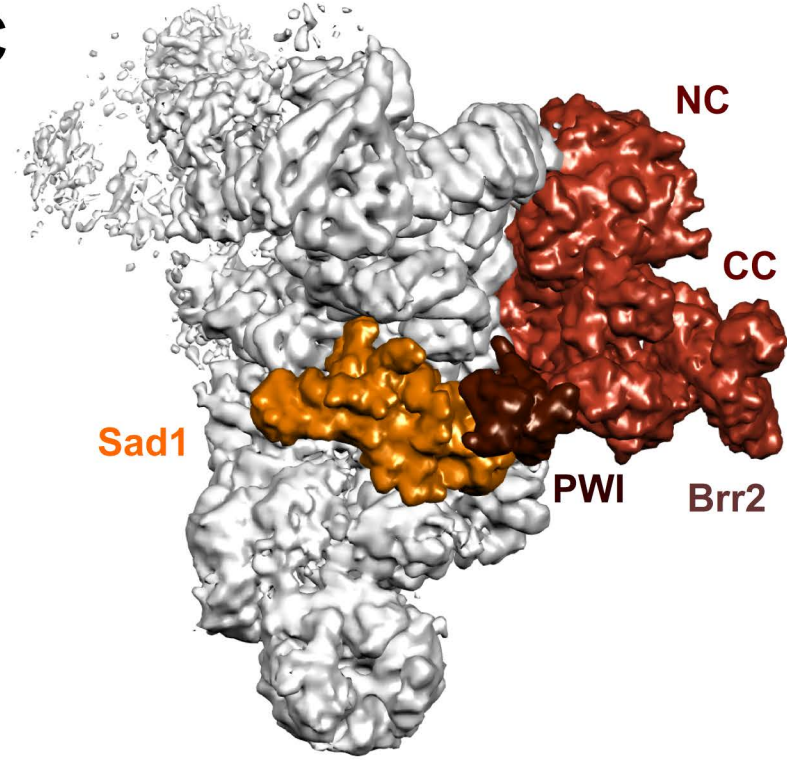
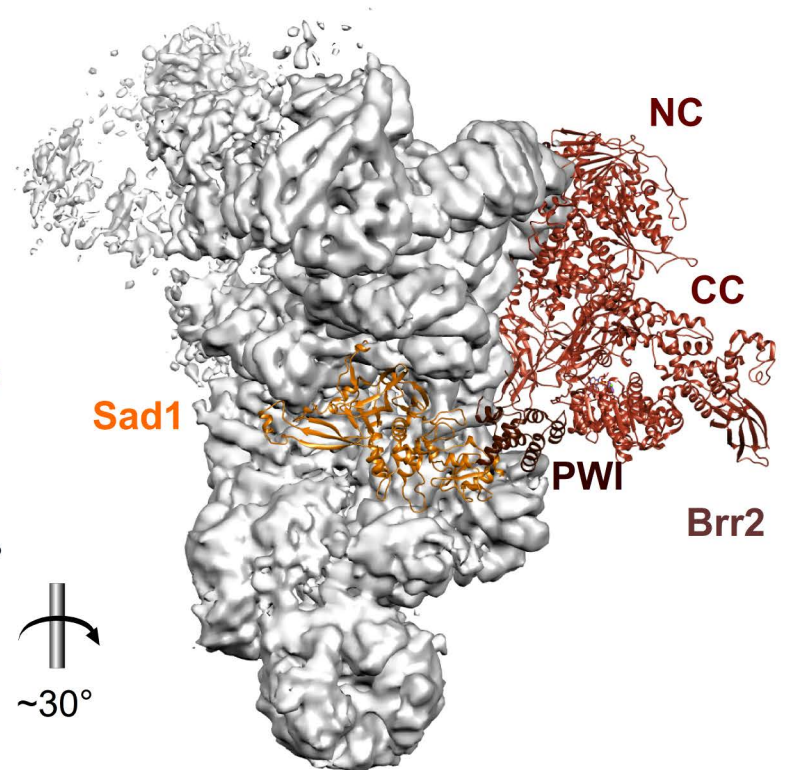
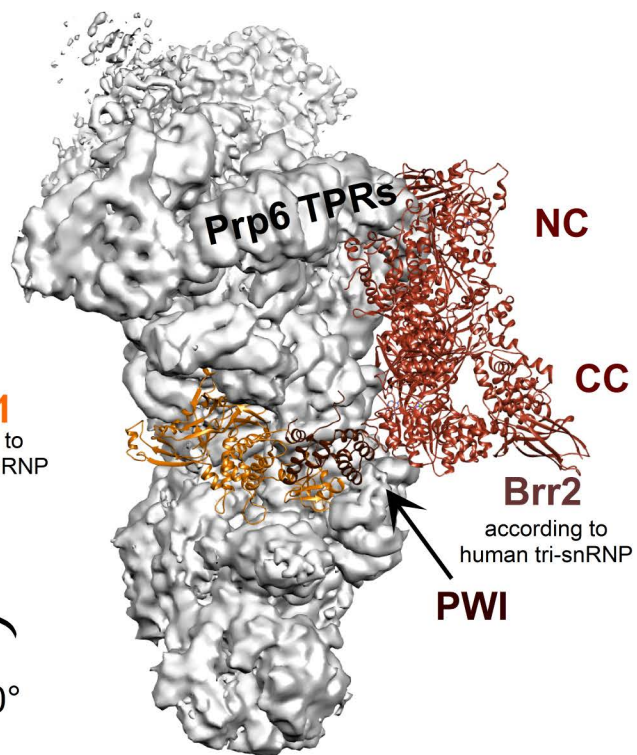
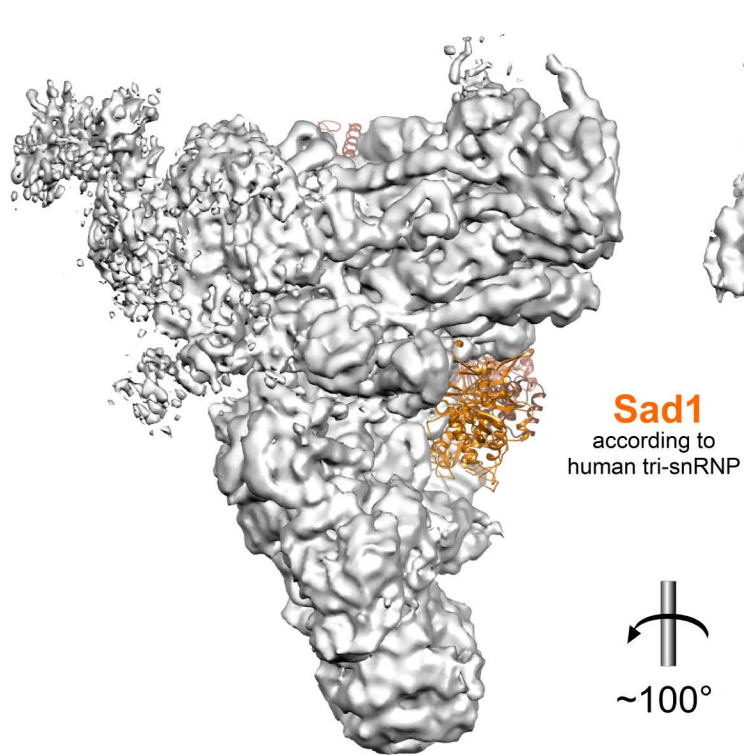
Cryo-EM 3D structure from  
crosslinked tri-snRNPs

3D structure from non crosslinked  
negative stain EM data

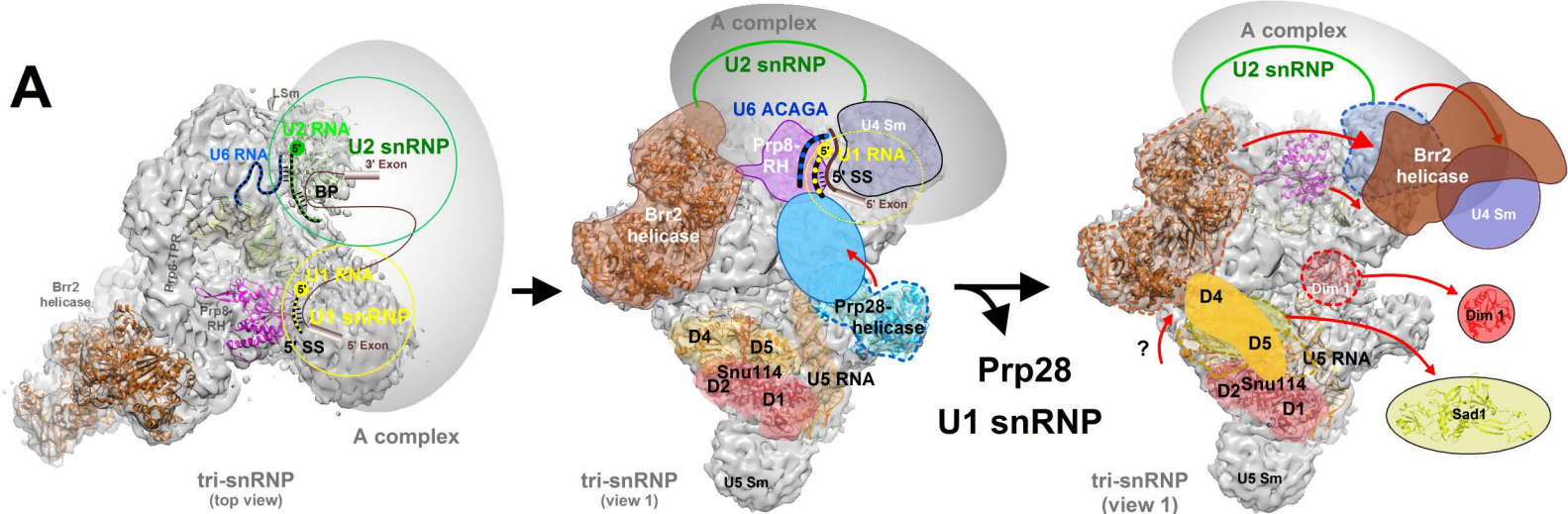
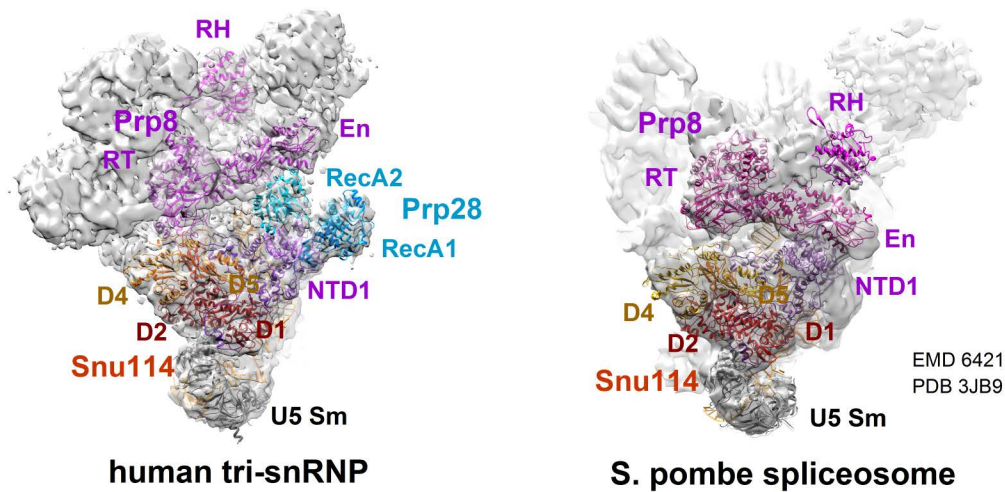
**Figure S12. Superposition of the 3D cryo-EM structures of the human and yeast tri-snRNPs.** (A and C) Views from the top of the 3D structures of the human (red; for clarity reasons shown at 9.5 Å resolution) and *S. cerevisiae* (green) tri-snRNP, which are superpositioned in (B). The small diagrams on the left are the corresponding side views. The 3D structures are aligned such that the 3D structures of the U5 proteins Prp8 and Snu114 and the U5 Sm core structure are brought into alignment. Superpositioning reveals the large difference in the positions of Brr2 and the U4 Sm core in the two models. At the same time, relative to the “long axis” of Prp8 (i.e. going from “RT” to “En”), which is the same in all three representations, the U4/U6 proteins and Prp6 are closer to the RT domain in the yeast versus human tri-snRNP.



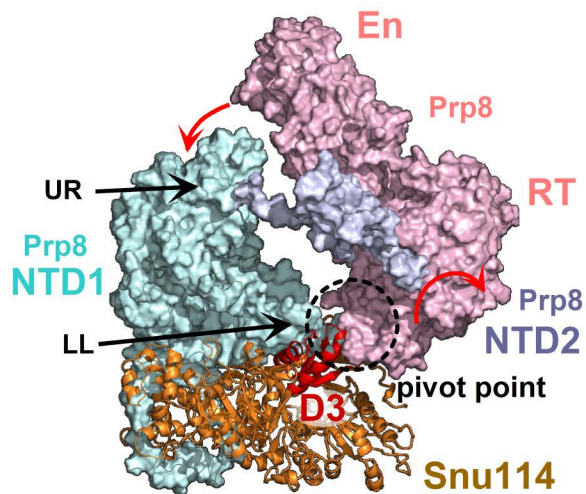
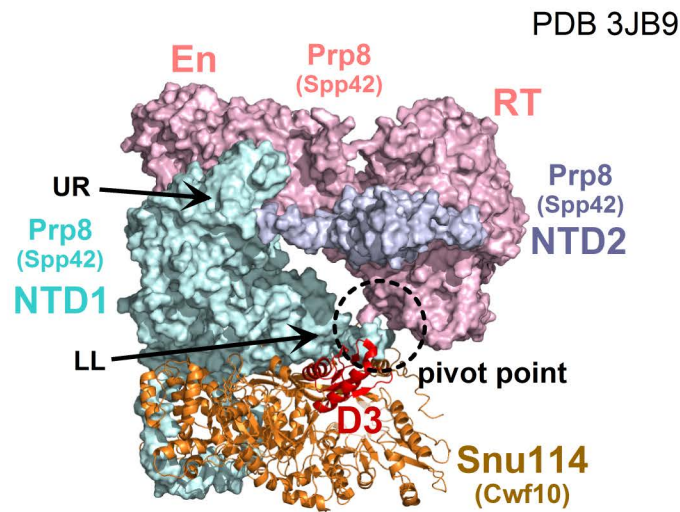
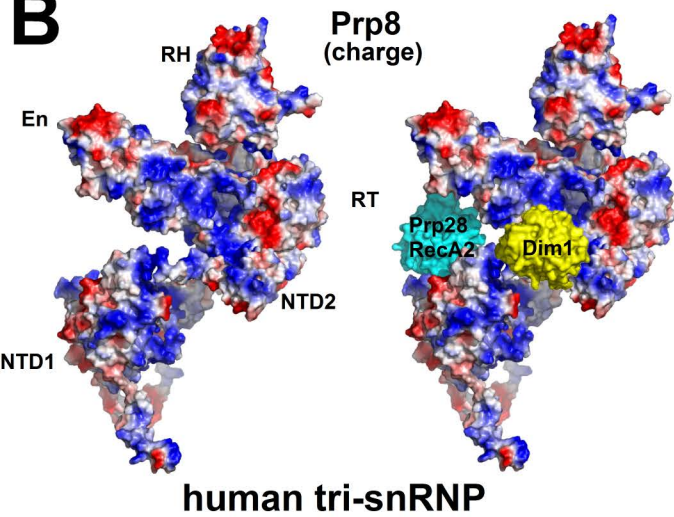
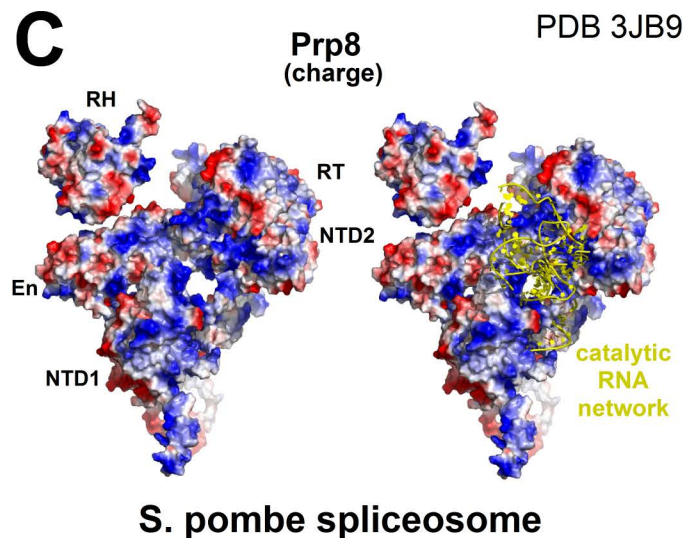
**Figure S13. Brr2 and Sad1 can be docked at the corresponding positions in the yeast tri-snRNP 3D structure where they are found in the human tri-snRNP.** (A) The *S. cerevisiae* cryo-EM 3D structure (9) is constricted in the central part. (B) The Brr2 tandem helicase domain (bound to Jab1) and the Sad1 protein, which is connected by Brr2's PWI domain in the human tri-snRNP (Fig. 5), fit together as a rigid body into matching cavities of the yeast tri-snRNP structure. The fit includes the same Brr2-Sad1 positioning relative to Prp8 and Snu114 as found in the human tri-snRNP structure. In the different views it can be seen that there are only minor clashes upon docking of these proteins, mainly at the N-terminal TPRs of Prp6. (C) Space filling presentation of Sad1 and Brr2 illustrating the good spatial fit.

**A****C****B**

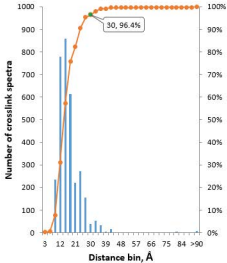
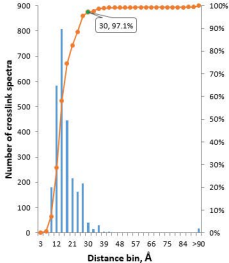
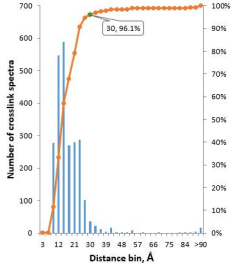
**Figure S14. Proposed sequential tri-snRNP remodeling steps during spliceosome assembly and activation.** (A) Left: Initial docking of the A complex (grey oval) at the top of the tri-snRNP, involving base pairing of U2 RNA (green dashed line) and U6 snRNA (blue dashed line), and association of Prp8's RH domain with U1 snRNA (yellow dashed line) based paired to the pre-mRNA 5' splice site (5'SS). Green and yellow circles: the U1 and U2 snRNP, respectively. Middle: Movement of Prp28 from its outward position through the cleft to the Prp8 RH domain where it mediates the handover of the 5'SS from U1 to U6 snRNA, leading to spliceosomal B complex formation. Right: Spliceosome activation requires Brr2 movement from its pre-activation position across the cleft to engage its U4/U6 snRNA substrate, which may be triggered by dissociation of Sad1. Snu114 might transiently undergo a structural change from a compact to a more extended form, which would require Brr2 movement away from its pre-activation position to prevent steric clashes with Snu114 domains D4. (B) Prp8 undergoes a substantial conformational change during catalytic activation of the spliceosome. While the overall-structure of Prp8's large N-terminal NTD1 domain is similar, the RT/En domain adopts a significantly different position in the human tri-snRNP (left) and *S. pombe* spliceosome (right).

**A****B**

**Figure S15. Prp8 undergoes a large structural change after tri-snRNP incorporation into the spliceosome.** (A) Prp8 undergoes a substantial conformational change during catalytic activation of the spliceosome. While the overall-structure of Prp8's large N-terminal NTD1 domain is similar, the RT/En domain adopts a significantly different position in the human tri-snRNP (left) and *S. pombe* spliceosome (right). In the tri-snRNP Prp8 is in an open conformation with the En-end of the elongated RT/En domain well-separated from the upper region (UR, helical region) of the NTD1 domain. The lower right region (LL, long loop, comprising amino acids V283 to R309) of NTD1, as well as the Snu114 D3 domain, are connected to the RT end of the RT/En domain and represent the pivot point around which the RT/En domain likely rotates (left). To achieve the spatial orientation observed in the *S. pombe* spliceosome (right) (10) where Prp8 is in a more closed conformation, the RT/En domain must move toward the NTD1 domain, such that the En domain now tightly contacts the NTD1 at the UR site. The RT/En domain must not only tilt around the pivot point (the RT-LL interface) along its long axis but also along its short axis. As a result of these movements, the RT-LL interface is greatly reduced and the RT contact to Snu114-D3 present in the tri-snRNP is not maintained in the *S. pombe* spliceosome. Surface charge representation of Prp8 in the human tri-snRNP (B) or *S. pombe* spliceosome (C), where blue represents positively-charged and red negatively-charged residues. The open Prp8 conformation in the human tri-snRNP (B) provides binding sites for the Dim1 protein and the Prp28-RecA2 domain. The Dim1-binding region of Prp8 is highly positively-charged and encompasses the RT/En-NTD1-NTD2 interface region. Binding of these proteins likely prevents Prp8 from adopting the closed conformation observed in the *S. pombe* spliceosome (C). The closed conformation generates the binding pocket for the catalytic RNA network that is formed during catalytic activation (C, right) (32).

**A****human tri-snRNP****S. pombe spliceosome****B****C**

**Figure S16. Distribution of the C $\alpha$ -C $\alpha$  distances between BS3-crosslinked residues.**  
The Euclidian distances were measured in the 7 Å model of the human tri-snRNP using PyMOL 1.7. More than 95% of all crosslink-assigned spectra correspond to crosslink distances of 30 Å or less.

**Set 1****Set 2****Set 3**

Number of crosslink spectra Cumulative %

## Supplementary Tables

**Table S1: Protein and model building information for all modeled tri-snRNP proteins.** Protein names, their molecular weight and detailed information about the model building process are provided. The correlation coefficient was calculated as the correlation between the simulated 7 Å 3D map of each protein domain and the experimental EM 3D density map using the commands "molmap" and "measure correlation" of UCSF Chimera (43).

**Table S2: BS3-crosslinks between and within known structured regions of human tri-snRNP proteins**

Statistics (Spectral Counts and Score<sub>max</sub>) of the CX-MS data for the proteins of the purified human tri-snRNP. "Inter" and "Intra" indicate inter-protein and intra-protein crosslinks, respectively. Numbers in the Residue 1 and 2 columns indicate the position of the crosslinked lysine or N-terminal methionine residue.

**Table S1. Positioning of proteins in the human tri-snRNP cryo-EM 3D structure**

Protein Names	MW Length	Domain	Amino Acids	Structure Source	Reference	Note	Correlation coefficient	Positioning in the tri-snRNP cryo-EM 3D structure
hPrp8 U5-220K	273.6 kDa 2335	NTD1	26-662	S.p. 34-685 (Spp42) PDB 3JB9	(10)	orthologue model (Swiss Model)	0.874	The structure of the N-terminal domain (NTD) of Prp8 in the <i>S. pombe</i> spliceosome was recently solved by Cryo-EM (10). Based on this structure, we have divided the NTD into a large domain (NTD1) at the very N terminus, a downstream linker (NTDL) and remaining C-terminal region (NTD2). In the <i>S. pombe</i> spliceosome NTD1 is largely $\alpha$ -helical and compact, but on one side a long, mostly unstructured region (between M271 and N397 in the human orthologue) protrudes, with its two loops oriented in different directions. An unstructured linker also connects the helix at the very beginning of NTD1 to the globular main NTD1 body. The homology-modeled NTD1 structure fits very well into a density of the tri-snRNP 3D structure located in the lower part close to U5 stem-loop 1, which is largely covered by the helical region. The lasso-shaped loop of the large unstructured region fits into a circular density surrounding Snu114-D1 (fig. S8B) and the other loop (named long loop, LL; V283-R309) runs above Snu114-D4-D5 (fig. S15A). When this NTD1 is fitted as a rigid body into the density, the N-terminal helix is positioned close to the U5-40K WD40 protein. The overall position of NTD1 in the tri-snRNP is extremely similar to that found in the <i>S. pombe</i> spliceosome (10). Only the N-terminal helix has to be moved somewhat – into a density element above the U5-40K WD40 domain – to attain the corresponding <i>S. pombe</i> position (fig. S8C). Several crosslinks support this location (K29, K36, K43, K48, K50 of U5-40K-WD40 to K286 and/or K349 of NTD1).
		NTDL NTD2	663-677 678-798	S.p. 686-821 (Spp42) PDB 3JB9	(10)	orthologue model (Swiss Model)	0.813	In the <i>S. pombe</i> spliceosome structure, the NTDL, which is about 15 amino acids long, spans the gap between NTD1 and NTD2. The latter is small and contains four helices that are attached to the RT region of Prp8. In the tri-snRNP the two C-terminal helices of the homology-modeled NTD2 fit very well into density elements positioned relative to the RT domain in the same way as found in the <i>S. pombe</i> spliceosome. The two N-terminal helices of NTD2 are arranged in a V-like manner. Close by there are two similarly arranged densities, into which the two helices can be fitted perfectly by twisting them around the connection between the second N-terminal helix and the first C-terminal helix by about 30 degrees. As in the <i>S. pombe</i> spliceosome, the Prp8-RT/En domain is positioned relative to the NTD1 domain quite differently compared to the situation in the human tri-snRNP (figs. S14 and S15); the RT-attached NTD2 is also differently positioned with respect to NTD1. Therefore, the NTDL linking NTD1 and NTD2 has to be tilted to reach the NTD1-C-terminus to which it connects. A density for the stretched NTDL sequence is barely visible, but a number of crosslinks determine its likely path (fig. S8A). Several crosslinks also confirm the NTD2 positioning close to the RT domain (fig. S8A).
		Prp8-RT/En	799-1755	S.p. 821-1779 (Spp42) PDB 3JB9	(10)	orthologue model (Swiss Model)	0.844	In the ca. 12 nm long RT/En domain, the En and linker domains form, together with the thumb helices of the RT domain, a slightly twisted tail that originates from the ca. 7 nm broad RT ‘head’ structure. In the cryo-EM reconstruction of the human tri-snRNP, the tapered wedge-like RT/En structure fits into a correspondingly-shaped density element at the center of the particle (Fig. 3A). The broad RT side is positioned in a region surrounded by large density elements, while the pointed En end protrudes slightly up and outwards at the periphery of the tri-snRNP, ending just below the U4 Sm complex. The model based on the <i>S. pombe</i> orthologue (Spp42) structure in the late spliceosome (10) gives a better fit than the model based on the <i>S. cerevisiae</i> Prp8 crystal structure (44). The spliceosome catalytic core site of the RT/En structure, where the rearranged catalytic U2/U6 snRNA network and U5 snRNA loop 1 dock, faces almost directly the U4/U6 three-way junction, but is well separated from it. The U5 stem-loop 1 is located just below the RT-linker region, with the loop closest to the RT-thumb helices.
		Prp8-RH	1760-2015	PDB 3E9L	(45)	crystal structure	0.910	The Prp8-RH domain was placed close to Prp8’s RT/En domain into a well-fitting density element by initially keeping the arrangement found in the Prp8-Aar2 co-crystal (44). Compared with the crystal structure, only a small shift and a rotation around the axis along the RH $\beta$ -finger are necessary to achieve a very good fit (see also Fig.3A and fig. S7). In this fit, the $\beta$ -finger is well-positioned in a small, elongated, protruding density region. Thus, the RH domain is situated centrally at the top of the tri-snRNP with the presumed RNA-binding surface oriented towards the space between the U4 Sm complex and the RT domain. The RH domain is connected to the RT domain by a density band that extends up to the arc that bridges the RH domain and the U4/U6 site. For intermolecular crosslinks of the RH domain with other tri-snRNP proteins see fig. S9.
		Prp8-Jab1	2067-2335	PDB 4KIT	(20)	co-crystal with Brr2	0.902	The Prp8-Jab1 domain was inserted into the tri-snRNP reconstruction by straightforward positioning of the Brr2-Jab1 co-crystal structure (20). As described in more detail in fig. S9, taking our intra- and intermolecular crosslinks into account we have also positioned part of the linker region connecting the Jab1 and Prp8 RH domains, close to the Jab1 domain.
hBrr2 U5-200K SNRNP200	244.5 kDa 2136	Brr2-helicase	404-2125	PDB 4KIT	(20)	N-terminal (NC) and C-Terminal (CC)	0.919	For the large co-crystal structure of Brr2’s entire helicase region in complex with Prp8’s Jab1 domain (20), a perfectly fitting peripheral density region positioned at the RT end of Prp8’s RT/En structure is clearly apparent. In this fit, the C-terminal (inactive) helicase cassette takes up a peripheral position, whereby its Ig domain is the

						helicase cassette co-crystal with Prp8-Jab1		most highly exposed external structural element. The N-terminal (active) cassette has a more central position, with the Jab1 domain pointing downwards in the direction of Snu114. The almost perfect fit of the co-crystal structure of the helicase cassettes and the Jab1 domain into the tri-snRNP density indicates that the structure of the [Brr2-Jab1] complex in the tri-snRNP is well reflected in its compact crystal structure. Only the position of a small helix (T1967-G1978) close to the C-terminus was slightly adjusted to fit into a close-by density element.
		Brr2-PWI	249-368	C.t. 287-422, PDB 4RVQ	(22)	orthologue model (Swiss Model)	0.893	The crystal structure of the non-canonical, evolutionarily conserved PWI domain from <i>C. thermophilum</i> , comprising amino acids 249 to 365 in the N-terminal region of human Brr2, fits very well into a density element connecting Brr2's C-terminal cassette (CC) to the proteins Snu114 and Sad1. This is entirely consistent with intermolecular crosslinks between these domains (for details see Fig. 5B and fig. S10). The PWI domain represents the major point of attachment of the C-terminal cassette to the tri-snRNP.
		Brr2-NHD	83-179	S.c. 113-192 PDB 5DCA	(23)	orthologue model (Swiss Model)	0.877	The N-terminal region of Brr2 has been proposed to contain a helical domain (henceforth termed NHD) (46). Recently, the crystal structure of a four-helices-containing bundle of this domain, called the plug, was solved (23). This structure fits well into the density element between the RecA2 and HB domains of Brr2's NC, and connects the NC to Prp8's RH domain and to TPR repeats of Prp6 closest to its N terminus. This density element contains a fifth rod-like density suitable for an $\alpha$ -helix, into which we have placed a helix modeled by the Robetta server for the N-terminal extension of the plug. The intramolecular crosslinks within this Brr2 region (table S2), as well as the intermolecular crosslinks between the Brr2-NHD domain and other neighboring protein domains are entirely consistent with the Brr2-NHD model and its position in the tri-snRNP (Fig. 4C and fig. S9).

hSnu114 U5-116K EFTUD2	109.4 kDa 972	Snu114-D1-D2	109-581	S.p. 121-595 (Cwf10) PDB 3JB9	(10)	orthologue model (Swiss Model)	0.858	With the exception of its N-terminal 115-residue domain, the 116-kDa protein Snu114 is highly homologous to the ribosomal translocase (elongation factor EF-2/EF-G). For modelling of the human Snu114 domains, we used the structure of the Snu144 orthologue Cwf10 observed in the <i>S. pombe</i> spliceosome (10). According to the numerous ribosomal translocase crystal structures, domains D1 and D2 represent a relatively rigid building block. In the tri-snRNP reconstruction, these two domains were placed into a well-fitting density region at the bottom of the particle just above the U5 Sm ring, with D1 proximal to U5 snRNA and D2 distal to it. The nucleotide-binding site is then oriented inwardly, in the direction of the U5 snRNA stem-loop 1 (5'SL).
		Snu114-D4-D5- C-terminal domain	663-957	S.p. 676-971 (Cwf10) PDB 3JB9	(10)	orthologue model (Swiss Model)	0.885	Based on the many ribosomal translocase crystal structures, domains D4 and D5 likewise represent a fairly rigid building block. These two domains were placed into a well-fitting density region at the bottom of the particle just above the D1-D2 block (see above). D5 was positioned above the center of D1-D2. D4 is on the D2 side, but is rotated about 30° to the outside, thus becoming positioned below the C-terminal cassette of Brr2 (Fig. 3).
		Snu114-D3	582-662	S.p. 596-675 (Cwf10) PDB 3JB9	(10)	orthologue model (Swiss Model)	0.813	The remaining D3 domain fits well into a density element that connects D2 with D4 domains. D3 is located in the center of the lower part of the tri-snRNP, below Prp8-RT (Fig. 3A).
U5-40K SNRNP40	39.3 kDa 357	40K-WD40	56-357	PFAM WD40	(46)	comparative (SpliProt3D)	0.901	A ring-shaped density element suitable for a WD40 propeller structure is present at the lower part of the 5'SL of U5 snRNA. Of the U5 proteins, only 40K contains a WD40 domain, and a modeled U5-40K structure fits well into this element (fig. S8C).
hDim1 U5-15K TXNL4A	16.8 kDa 142	Dim1	3-137	PDB 1QGV	(47)	crystal structure	0.872	For the small Dim1 protein, 8 crosslinks to the Prp8 domains RT/En or NTD2 were detected (fig. S8A). There is only one density, a nodule-like multiply interconnected element just between the three-way junction and the U5 snRNA and very close to the site where the catalytic center will form, into which the Dim1 protein fits well while allowing the formation of all the crosslinks (Fig. 3B).
hPrp28 U5-100k DDX23	95.6 kDa 820	Prp28-RecA2	630-806	PDB 4NHO	(17)	crystal structure	0.850	Several crosslinks from lysines within the C-terminal RecA2 domain of the Prp28 helicase to Prp8's RT/En and NTD1 (fig. S8A) place this C-terminal helicase region in a small density element below the Prp8-RT/En tip where it is positioned in a deep groove running horizontally between the Snu114 D4-D5 domains and the Prp8 RT/En domain (Fig. 3C).
		Prp28-RecA1	352-629	PDB 4NHO	(17)	crystal structure	0.904	The Prp28-RecA1 domain must be located in close proximity to the C-terminal RecA2 domain, because the linker connecting them is short. The RecA1 domain fits into a knob-like protuberance linked to the density element containing Prp28-RecA2 (Fig. 3C). This arrangement indicates that the Prp28 helicase adopts an inactive, open conformation in the tri-snRNP, which is consistent with our finding that in the isolated tri-snRNP Prp28 cannot bind ATP (17). All available crystal structures of the isolated Prp28 helicase also show an open conformation, in which the two RecA-like domains are turned away from one another.
hPrp6 U5-102K	106.9 kDa 941	Prp6-TPR	291-941	PFAM HAT	(46)	comparative (SpliProt3D)	0.891	Our analysis revealed a deep cleft between the U5 and U4/U6 domains in the tri-snRNP; only a few defined bridges seem to connect the proteins of these two snRNPs. The most remarkable feature is an arc-like bridge at

ANT-1 PRPF6								the top that straddles the cleft as a ribbon-like structure. The size of the ribbon has striking similarities to chains of $\alpha$ -helical TPRs. Prp6 is the only tri-snRNP protein in which the sequence indicates extended TPR repeats. Most of its 19 repeats are also confirmed by intramolecular crosslinks, and the intermolecular crosslinks establish that Prp6 bridges U5 and U4/U6 proteins and define the chain polarity, as illustrated in Fig. 2B and fig. S4. The N-terminus of the TPR ribbon interacts first with the Prp8 RT and RH domains, and two TPRs later it also contacts the N-terminal cassette of Brr2. It then forms a bridge that connects to the U4/U6 site, connecting all of the known structural modules of Prp3, Prp4, Prp31 and 15.5K by forming a circle that involves the C-terminal most seven of its 19 TPRs.
hPrp3 U4/U6-90K PRPF3	77.5 kDa 683	Prp3-CTF (DUF1115)	539-673	S.c. 296-469, PDB 4YHW	(48)	U6 RNA binding domain co-crystal with U4/U6 RNA orthologue model (Swiss Model)	0.839	Superimposition of the U4/U6 stem II RNA helix of the co-crystal structure containing the C-terminal fragment of Prp3 (Prp3-CTF) (48) onto the U4/U6 stem II density of the tri-snRNP 3D structure places the U6 snRNA-bound Prp3 domain into a larger density in an upper corner of the tri-snRNP (Fig. 2A). In the crystal structure, Prp3 is primarily bound to the 8 nucleotides of U6 snRNA that are immediately adjacent to U4/U6 stem II on the 3' side (see fig. S1C). The 3' end of this U6 region now becomes positioned just in front of the LSm site that binds the extreme 3' end of the U6 snRNA.
hPrp31 U4/U6-61K NY-BR-99 PRPF31	55.5 kDa 499	Prp31	85-333	PDB 2OZB	(49)	co-crystal with 15.5K and U4RNA K-turn	0.915	The Prp31 domain has an arc-like structure with two long helices bridging the Snu13-bound Nop domain to the coiled-coil tip structure. Its crystal structure (49) fits very well into a diagonal, downward-running and arc-shaped density at the outer surface of the tri-snRNP (Fig. 2A). The Nop-domain pillar of the bridge points toward the Dim1 protein, while the other (coiled-coil) pillar is attached to the Sad1-UCH domain (Fig. 5).
hSnu13 U4/U6-15.5K NHP2L1	14.2 kDa 128	Snu13	3-128	PDB 2OZB	(49)	co-crystal with Prp31 and U4RNA K-turn	0.894	The position and orientation of the K-turn also defines the positions of the two proteins of the co-crystal structure. Snu13 is bound directly to the K-turn at the end of U4 5'SL, and we thus place it between the K-turn and stem II of U4/U6 (Fig. 2A).
hPrp4 U4/U6-60K Q5T1M7 PRPF4	58.3 kDa 521	Prp4-WD40	215-521	PFAM WD40	(46)	comparative (SpliProt3D)	0.896	The C-terminal WD40 domain of Prp4 fits into a ring-shaped region of the large density that harbors the other U4/U6 proteins - Prp3, Prp31, Snu13 and the LSm heptamer (Fig 2).
CypH U4/U6-20K PPIaseH PPIH	19.2 kDa 177	CypH	5-177	PDB 1MZW	(50)	co-crystal with Prp4-107-137	0.805	The small cyclophilin H (CypH) protein is expected to be close to Prp4 because its crystal structure was solved with a bound Prp4 peptide. As K153 of CypH also crosslinks to K649 of the Prp3-CTF (table S2), we placed it in the density region that connects Prp4-WD40 and the Prp3 domain and also the LSm ring (Fig. 2A).
hSad1 U5.U4/U6-65K USP39 SNUT2	65.4 kDa 565	Sad1-Zf-UBP  Sad1-UCH	105-196  197-556	S.c. 29-124, PDB 4MSX  S.c. 125-448, PDB 4MSX	(51)	orthologue model (Swiss Model)	0.820	The Sad1 protein, with its two domains arranged exactly as in the crystal structure of the yeast protein (51), fits perfectly into a density below the Prp31 protein (Fig. 5). The density shape provides clear positions for the Zf-UBP domain and three UCH subdomains (palm, thumb and fingers). The palm, which harbors a lysine (K508) that crosslinks to Prp8 RT (K983) is positioned close to the respective site of the RT domain. The thumb points downwards into the particle and comes close to the D3 domain of Snu114, while the fingers run parallel to Prp8 NTD2 and their lysines crosslink in particular to the NTDL that links NTD2 to NTD1 (fig. S8A). Small helices were de novo modeled at the finger tips for sequences not present in the crystal structure (L360-E369 and I425-L438), and were placed into close-by densities. In the 3D reconstruction of the tri-snRNP, no density is present at the canonical ubiquitin-binding site located between the three subdomains of UCH. The Zf-UBP domain resides, as in the crystal structure, on the UCH-palm side and occupies a density surrounded by UCH, Prp8-RT, Brr2-PWI and the Snu114 domains D2, D3 and D4 (see also Fig. 5 and fig. S10 for further details and intermolecular crosslinks).

hSnu66 U5.U4/U6-110K Sart1, SNUT1	90.3 kDa 800							These proteins are largely unstructured and could not be assigned to a particular density in the 3D cryo EM structure of the tri-snRNP. This also applies to various low complexity regions of other tri-snRNP proteins, including the N-terminal regions of Prp3, Prp6 and Prp28 and the C-terminal region of Prp31.
27K U5.U4/U6-27K SNRNP27 SNUT3	18.8 kDa 155							
RBM42	50.4 kDa 480							

SmB SNRPB	24.6 kDa 240	SmB	6-95	PDB 4WZJ	(52)	co-crystal with SmD1,D2,D3,E,F, G, U4RNA	0.892 (U5) 0.856 (U4)	<p><b>U5 Sm</b> The 5' stem-loop (5'SL) is connected to the U5 Sm binding site by eight unpaired nucleotides that can easily bridge the 3' end of the 5'SL to the center of the large circular density at the very bottom of the tri-snRNP (Fig. 1B). In this density, the typical heptameric ring structure fits perfectly, in a tilted orientation, with the side containing the final 3' stem-loop facing diagonally downwards. The 5' m3G cap of the U5 snRNA is found directly at the lower end of the 5' stem. This position fits nicely with the result of an earlier localization by immuno-EM, in which it was found at the bottom of the particle (12).</p> <p><b>U4 Sm</b> At the top of the particle, a second Sm-shaped circular density element is present at some distance from the U4/U6 stem I site. Twenty one nucleotides are situated between the end of stem I and the stem-loop directly preceding the Sm binding site. This stretch is long enough to bridge the distance between the U4-Sm and the U4/U6 helix connection sites. The crystal structure of the U4 Sm core RNP fits well into the circular density (Fig. 1B). Protruding centrally on both sides, are smaller regions of density that can accommodate the two stem-loops of U4 snRNA that flank the Sm site. The U4 Sm ring is tilted just above the Prp8-En end of the RT/En domain, with its flat side, containing the penultimate stem-loop, pointing outwards (like the RT/En domain).</p>
SmD1 SNRPD1	13.3 119	SmD1	2-95	PDB 4WZJ	(52)	co-crystal with SmB,D2,D3,E,F,G, U4RNA		
SmD2 SNRPD2	13.5 kDa 118	SmD2	26-114	PDB 4WZJ	(52)	co-crystal with SmB,D1,D3,E,F,G, U4RNA		
SmD3 SNRPD3	13.9 kDa 126	SmD3	4-91	PDB 4WZJ	(52)	co-crystal with SmB,D1,D2,E,F,G, U4RNA		
SmF RUXF SNRPF	9.7 kDa 86	SmF	4-86	PDB 4WZJ	(52)	co-crystal with SmB,D1,D2,D3,E, G, U4RNA		
SmE SNRPE	10.8 kDa 92	SmE	15-92	PDB 4WZJ	(52)	co-crystal with SmB,D1,D2,D3,F, G, U4RNA		
SmG RUXG SNRPG	8.5 kDa 76	SmG	4-76	PDB 4WZJ	(52)	co-crystal with SmB,D1,D2,D3,E,F , U4RNA		
LSm2	10.8 kDa 95	LSm2	1-90	S.c. 1-90 PDB 4M7A	(53)	co-crystal with LSm3,4,5,6,7,8, U6RNA orthologue model (Swiss Model)	0.897	<p>The 3' end of U6 snRNA extends from the U4/U6 stem II. The single-stranded sequence is first bound to the Prp3-CTF (48) which is located at the top of the tri-snRNP, and at its extreme 3' end to the heptameric LSm ring. A well-fitting ring-shaped density is seen directly adjacent to the Prp3 domain at the top of the particle. Here the U6 LSm ring fits perfectly, with its flat RNA-binding side directly and centrally facing the U6 snRNA that is bound to, and protrudes from, Prp3. The U6 sequence connecting the LSm- and Prp3-bound sequences contains the stretch of U6 that base pairs with the 5' end of U2 snRNA during B complex formation (fig. S1). It is also located at this exposed corner of the tri-snRNP.</p>
LSm3	11.8 kDa 102	LSm3	16-98	S.c. 3-79 PDB 4M7A	(53)	co-crystal with LSm2,4,5,6,7,8, U6RNA orthologue model (Swiss Model)		
LSm4	15.4 kDa 139	LSm4	1-80	S.c. 1-90 PDB 4M7A	(53)	co-crystal with LSm2,3,5,6,7,8, U6RNA orthologue model (Swiss Model)		
LSm5	9.9 kDa 91	LSm5	10-85	S.c. 4-84 PDB 4M7A	(53)	co-crystal with LSm2,3,4,6,7,8, U6RNA orthologue model (Swiss Model)		
LSm6	9.1 kDa 80	LSm6	7-76	S.c. 11-84 PDB 4M7A	(53)	co-crystal with LSm2,3,4,5,7,8, U6RNA orthologue model (Swiss Model)		
LSm7	11.6 kDa 103	LSm7	11-89	S.pombe. 24- 101 PDB 4EMK	(54)	co-crystal with LSm5,6,7 orthologue model (Swiss Model)		
LSm8 NAA38	10.4 kDa 96	LSm8	4-73	S.c. 4-67 PDB 4M7A	(53)	co-crystal with LSm2,3,4,5,6,7, U6RNA orthologue model (Swiss Model)		

**Movie S1.** The movie shows the tri-snRNP 3D structure rotating along its long axis. The fitted proteins and RNA parts of the tri-snRNP are shown in the semi-transparent envelope of the EM density.

## References

1. M. C. Wahl, C. L. Will, R. Lührmann, The spliceosome: Design principles of a dynamic RNP machine. *Cell* **136**, 701–718 (2009). [Medline doi:10.1016/j.cell.2009.02.009](#)
2. T. W. Nilsen, in *RNA Structure and Function*, R. Simons, M. Grunberg-Manago, Eds. (Cold Spring Harbor Laboratory Press, Cold Spring Harbor, NY, 1998), pp. 279–307.
3. S. M. Fica, M. A. Mefford, J. A. Piccirilli, J. P. Staley, Evidence for a group II intron-like catalytic triplex in the spliceosome. *Nat. Struct. Mol. Biol.* **21**, 464–471 (2014). [Medline doi:10.1038/nsmb.2815](#)
4. T. Achsel, K. Ahrens, H. Brahms, S. Teigelkamp, R. Lührmann, The human U5-220kD protein (hPrp8) forms a stable RNA-free complex with several U5-specific proteins, including an RNA unwindase, a homologue of ribosomal elongation factor EF-2, and a novel WD-40 protein. *Mol. Cell. Biol.* **18**, 6756–6766 (1998). [Medline doi:10.1128/MCB.18.11.6756](#)
5. W. P. Galej, T. H. D. Nguyen, A. J. Newman, K. Nagai, Structural studies of the spliceosome: Zooming into the heart of the machine. *Curr. Opin. Struct. Biol.* **25**, 57–66 (2014). [Medline doi:10.1016/j.sbi.2013.12.002](#)
6. R. J. Grainger, J. D. Beggs, Prp8 protein: At the heart of the spliceosome. *RNA* **11**, 533–557 (2005). [Medline doi:10.1261/rna.2220705](#)
7. B. Laggerbauer, T. Achsel, R. Lührmann, The human U5-200kD DEXH-box protein unwinds U4/U6 RNA duplexes in vitro. *Proc. Natl. Acad. Sci. U.S.A.* **95**, 4188–4192 (1998). [Medline doi:10.1073/pnas.95.8.4188](#)
8. P. L. Raghunathan, C. Guthrie, RNA unwinding in U4/U6 snRNPs requires ATP hydrolysis and the DEIH-box splicing factor Brr2. *Curr. Biol.* **8**, 847–855 (1998). [Medline doi:10.1016/S0960-9822\(07\)00345-4](#)
9. T. H. D. Nguyen, W. P. Galej, X. C. Bai, C. G. Savva, A. J. Newman, S. H. Scheres, K. Nagai, The architecture of the spliceosomal U4/U6.U5 tri-snRNP. *Nature* **523**, 47–52 (2015). [Medline doi:10.1038/nature14548](#)
10. C. Yan, J. Hang, R. Wan, M. Huang, C. C. Wong, Y. Shi, Structure of a yeast spliceosome at 3.6-angstrom resolution. *Science* **349**, 1182–1191 (2015). [Medline doi:10.1126/science.aac7629](#)

11. B. Kastner, N. Fischer, M. M. Golas, B. Sander, P. Dube, D. Boehringer, K. Hartmuth, J. Deckert, F. Hauer, E. Wolf, H. Uchtenhagen, H. Urlaub, F. Herzog, J. M. Peters, D. Poerschke, R. Lührmann, H. Stark, GraFix: Sample preparation for single-particle electron cryomicroscopy. *Nat. Methods* **5**, 53–55 (2008). [Medline doi:10.1038/nmeth1139](#)
12. B. Sander, M. M. Golas, E. M. Makarov, H. Brahms, B. Kastner, R. Lührmann, H. Stark, Organization of core spliceosomal components U5 snRNA loop I and U4/U6 Di-snRNP within U4/U6.U5 Tri-snRNP as revealed by electron cryomicroscopy. *Mol. Cell* **24**, 267–278 (2006). [Medline doi:10.1016/j.molcel.2006.08.021](#)
13. E. M. Makarov, O. V. Makarova, T. Achsel, R. Lührmann, The human homologue of the yeast splicing factor prp6p contains multiple TPR elements and is stably associated with the U5 snRNP via protein-protein interactions. *J. Mol. Biol.* **298**, 567–575 (2000). [Medline doi:10.1006/jmbi.2000.3685](#)
14. F. Galisson, P. Legrain, The biochemical defects of prp4-1 and prp6-1 yeast splicing mutants reveal that the PRP6 protein is required for the accumulation of the [U4/U6.U5] tri-snRNP. *Nucleic Acids Res.* **21**, 1555–1562 (1993). [Medline doi:10.1093/nar/21.7.1555](#)
15. P. Fabrizio, B. Laggerbauer, J. Lauber, W. S. Lane, R. Lührmann, An evolutionarily conserved U5 snRNP-specific protein is a GTP-binding factor closely related to the ribosomal translocase EF-2. *EMBO J.* **16**, 4092–4106 (1997). [Medline doi:10.1093/emboj/16.13.4092](#)
16. R. Jørgensen, P. A. Ortiz, A. Carr-Schmid, P. Nissen, T. G. Kinzy, G. R. Andersen, Two crystal structures demonstrate large conformational changes in the eukaryotic ribosomal translocase. *Nat. Struct. Biol.* **10**, 379–385 (2003). [Medline doi:10.1038/nsb923](#)
17. S. Möhlmann, R. Mathew, P. Neumann, A. Schmitt, R. Lührmann, R. Ficner, Structural and functional analysis of the human spliceosomal DEAD-box helicase Prp28. *Acta Crystallogr. D* **70**, 1622–1630 (2014). [Medline doi:10.1107/S1399004714006439](#)
18. A. Jacewicz, B. Schwer, P. Smith, S. Shuman, Crystal structure, mutational analysis and RNA-dependent ATPase activity of the yeast DEAD-box pre-mRNA splicing factor Prp28. *Nucleic Acids Res.* **42**, 12885–12898 (2014). [Medline doi:10.1093/nar/gku930](#)
19. K. F. Santos, S. M. Jovin, G. Weber, V. Pena, R. Lührmann, M. C. Wahl, Structural basis for functional cooperation between tandem helicase cassettes in Brr2-mediated remodeling of the spliceosome. *Proc. Natl. Acad. Sci. U.S.A.* **109**, 17418–17423 (2012). [Medline doi:10.1073/pnas.1208098109](#)
20. S. Mozaffari-Jovin, T. Wandersleben, K. F. Santos, C. L. Will, R. Lührmann, M. C. Wahl, Inhibition of RNA helicase Brr2 by the C-terminal tail of the spliceosomal protein Prp8. *Science* **341**, 80–84 (2013). [Medline doi:10.1126/science.1237515](#)

21. C. Maeder, A. K. Kutach, C. Guthrie, ATP-dependent unwinding of U4/U6 snRNAs by the Brr2 helicase requires the C terminus of Prp8. *Nat. Struct. Mol. Biol.* **16**, 42–48 (2009). [Medline doi:10.1038/nsmb.1535](#)
22. E. Absmeier, L. Rosenberger, L. Apelt, C. Becke, K. F. Santos, U. Stelzl, M. C. Wahl, A noncanonical PWI domain in the N-terminal helicase-associated region of the spliceosomal Brr2 protein. *Acta Crystallogr. D* **71**, 762–771 (2015). [Medline doi:10.1107/S1399004715001005](#)
23. E. Absmeier, J. Wollenhaupt, S. Mozaffari-Jovin, C. Becke, C. T. Lee, M. Preussner, F. Heyd, H. Urlaub, R. Lührmann, K. F. Santos, M. C. Wahl, The large N-terminal region of the Brr2 RNA helicase guides productive spliceosome activation. *Genes Dev.* **29**, 2576–2587 (2015). [Medline](#)
24. S. Mozaffari-Jovin, K. F. Santos, H. H. Hsiao, C. L. Will, H. Urlaub, M. C. Wahl, R. Lührmann, The Prp8 RNase H-like domain inhibits Brr2-mediated U4/U6 snRNA unwinding by blocking Brr2 loading onto the U4 snRNA. *Genes Dev.* **26**, 2422–2434 (2012). [Medline doi:10.1101/gad.200949.112](#)
25. S. E. Behrens, R. Lührmann, Immunoaffinity purification of a [U4/U6.U5] tri-snRNP from human cells. *Genes Dev.* **5**, 1439–1452 (1991). [Medline doi:10.1101/gad.5.8.1439](#)
26. S. W. Stevens, I. Barta, H. Y. Ge, R. E. Moore, M. K. Young, T. D. Lee, J. Abelson, Biochemical and genetic analyses of the U5, U6, and U4/U6 x U5 small nuclear ribonucleoproteins from *Saccharomyces cerevisiae*. *RNA* **7**, 1543–1553 (2001). [Medline](#)
27. P. Fabrizio, S. Esser, B. Kastner, R. Lührmann, Isolation of *S. cerevisiae* snRNPs: Comparison of U1 and U4/U6.U5 to their human counterparts. *Science* **264**, 261–265 (1994). [Medline doi:10.1126/science.8146658](#)
28. Y.-H. Huang, C.-S. Chung, D.-I. Kao, T.-C. Kao, S.-C. Cheng, Sad1 counteracts Brr2-mediated dissociation of U4/U6.U5 in tri-snRNP homeostasis. *Mol. Cell. Biol.* **34**, 210–220 (2014). [Medline doi:10.1128/MCB.00837-13](#)
29. H. Stark, R. Lührmann, Cryo-electron microscopy of spliceosomal components. *Annu. Rev. Biophys. Biomol. Struct.* **35**, 435–457 (2006). [Medline doi:10.1146/annurev.biophys.35.040405.101953](#)
30. J. L. Reyes, E. H. Gustafson, H. R. Luo, M. J. Moore, M. M. Konarska, The C-terminal region of hPrp8 interacts with the conserved GU dinucleotide at the 5' splice site. *RNA* **5**, 167–179 (1999). [Medline doi:10.1017/S1355838299981785](#)
31. B. Sander, M. M. Golas, R. Lührmann, H. Stark, An approach for de novo structure determination of dynamic molecular assemblies by electron cryomicroscopy. *Structure* **18**, 667–676 (2010). [Medline doi:10.1016/j.str.2010.05.001](#)

32. J. Hang, R. Wan, C. Yan, Y. Shi, Structural basis of pre-mRNA splicing. *Science* **349**, 1191–1198 (2015). [Medline doi:10.1126/science.aac8159](#)
33. E. J. Sontheimer, J. A. Steitz, The U5 and U6 small nuclear RNAs as active site components of the spliceosome. *Science* **262**, 1989–1996 (1993). [Medline doi:10.1126/science.8266094](#)
34. E. C. Small, S. R. Leggett, A. A. Winans, J. P. Staley, The EF-G-like GTPase Snu114p regulates spliceosome dynamics mediated by Brr2p, a DExD/H box ATPase. *Mol. Cell* **23**, 389–399 (2006). [Medline doi:10.1016/j.molcel.2006.05.043](#)
35. C. M. T. Spahn, M. G. Gomez-Lorenzo, R. A. Grassucci, R. Jørgensen, G. R. Andersen, R. Beckmann, P. A. Penczek, J. P. Ballesta, J. Frank, Domain movements of elongation factor eEF2 and the eukaryotic 80S ribosome facilitate tRNA translocation. *EMBO J.* **23**, 1008–1019 (2004). [Medline doi:10.1038/sj.emboj.7600102](#)
36. J. Lin, M. G. Gagnon, D. Bulkley, T. A. Steitz, Conformational changes of elongation factor G on the ribosome during tRNA translocation. *Cell* **160**, 219–227 (2015). [Medline doi:10.1016/j.cell.2014.11.049](#)
37. J. D. Dignam, R. M. Lebovitz, R. G. Roeder, Accurate transcription initiation by RNA polymerase II in a soluble extract from isolated mammalian nuclei. *Nucleic Acids Res.* **11**, 1475–1489 (1983). [Medline doi:10.1093/nar/11.5.1475](#)
38. D. E. Agafonov, J. Deckert, E. Wolf, P. Odenwälder, S. Bessonov, C. L. Will, H. Urlaub, R. Lührmann, Semiquantitative proteomic analysis of the human spliceosome via a novel two-dimensional gel electrophoresis method. *Mol. Cell. Biol.* **31**, 2667–2682 (2011). [Medline doi:10.1128/MCB.05266-11](#)
39. A. Leitner, T. Walzthoeni, R. Aebersold, Lysine-specific chemical cross-linking of protein complexes and identification of cross-linking sites using LC-MS/MS and the xQuest/xProphet software pipeline. *Nat. Protoc.* **9**, 120–137 (2014). [Medline doi:10.1038/nprot.2013.168](#)
40. B. Yang, Y. J. Wu, M. Zhu, S. B. Fan, J. Lin, K. Zhang, S. Li, H. Chi, Y. X. Li, H. F. Chen, S. K. Luo, Y. H. Ding, L. H. Wang, Z. Hao, L. Y. Xiu, S. Chen, K. Ye, S. M. He, M. Q. Dong, Identification of cross-linked peptides from complex samples. *Nat. Methods* **9**, 904–906 (2012). [Medline doi:10.1038/nmeth.2099](#)
41. B. Sander, M. M. Golas, H. Stark, Automatic CTF correction for single particles based upon multivariate statistical analysis of individual power spectra. *J. Struct. Biol.* **142**, 392–401 (2003). [Medline doi:10.1016/S1047-8477\(03\)00072-8](#)
42. S. H. W. Scheres, RELION: Implementation of a Bayesian approach to cryo-EM structure determination. *J. Struct. Biol.* **180**, 519–530 (2012). [Medline doi:10.1016/j.jsb.2012.09.006](#)

43. E. F. Pettersen, T. D. Goddard, C. C. Huang, G. S. Couch, D. M. Greenblatt, E. C. Meng, T. E. Ferrin, UCSF Chimera—a visualization system for exploratory research and analysis. *J. Comput. Chem.* **25**, 1605–1612 (2004). [Medline doi:10.1002/jcc.20084](#)
44. W. P. Galej, C. Oubridge, A. J. Newman, K. Nagai, Crystal structure of Prp8 reveals active site cavity of the spliceosome. *Nature* **493**, 638–643 (2013). [Medline doi:10.1038/nature11843](#)
45. V. Pena, A. Rozov, P. Fabrizio, R. Lührmann, M. C. Wahl, Structure and function of an RNase H domain at the heart of the spliceosome. *EMBO J.* **27**, 2929–2940 (2008). [Medline doi:10.1038/emboj.2008.209](#)
46. I. Korneta, M. Magnus, J. M. Bujnicki, Structural bioinformatics of the human spliceosomal proteome. *Nucleic Acids Res.* **40**, 7046–7065 (2012). [Medline doi:10.1093/nar/gks347](#)
47. K. Reuter, S. Nottrott, P. Fabrizio, R. Lührmann, R. Ficner, Identification, characterization and crystal structure analysis of the human spliceosomal U5 snRNP-specific 15 kD protein. *J. Mol. Biol.* **294**, 515–525 (1999). [Medline doi:10.1006/jmbi.1999.3258](#)
48. S. Liu, S. Mozaffari-Jovin, J. Wollenhaupt, K. F. Santos, M. Theuser, S. Dunin-Horkawicz, P. Fabrizio, J. M. Bujnicki, R. Lührmann, M. C. Wahl, A composite double-/single-stranded RNA-binding region in protein Prp3 supports tri-snRNP stability and splicing. *eLife* **4**, e07320 (2015). 10.7554/eLife.07320 [Medline doi:10.7554/eLife.07320](#)
49. S. Liu, P. Li, O. Dybkov, S. Nottrott, K. Hartmuth, R. Lührmann, T. Carlomagno, M. C. Wahl, Binding of the human Prp31 Nop domain to a composite RNA-protein platform in U4 snRNP. *Science* **316**, 115–120 (2007). [Medline doi:10.1126/science.1137924](#)
50. U. Reidt, M. C. Wahl, D. Fasshauer, D. S. Horowitz, R. Lührmann, R. Ficner, Crystal structure of a complex between human spliceosomal cyclophilin H and a U4/U6 snRNP-60K peptide. *J. Mol. Biol.* **331**, 45–56 (2003). [Medline doi:10.1016/S0022-2836\(03\)00684-3](#)
51. H. Hadjivassiliou, O. S. Rosenberg, C. Guthrie, The crystal structure of *S. cerevisiae* Sad1, a catalytically inactive deubiquitinase that is broadly required for pre-mRNA splicing. *RNA* **20**, 656–669 (2014). [Medline doi:10.1261/rna.042838.113](#)
52. A. K. W. Leung, K. Nagai, J. Li, Structure of the spliceosomal U4 snRNP core domain and its implication for snRNP biogenesis. *Nature* **473**, 536–539 (2011). [Medline doi:10.1038/nature09956](#)
53. L. Zhou, J. Hang, Y. Zhou, R. Wan, G. Lu, P. Yin, C. Yan, Y. Shi, Crystal structures of the Lsm complex bound to the 3' end sequence of U6 small nuclear RNA. *Nature* **506**, 116–120 (2014). [Medline doi:10.1038/nature12803](#)

54. D. Wu, S. Jiang, M. W. Bowler, H. Song, Crystal structures of Lsm3, Lsm4 and Lsm5/6/7 from *Schizosaccharomyces pombe*. *PLOS ONE* **7**, e36768 (2012). [Medline](#)  
[doi:10.1371/journal.pone.0036768](https://doi.org/10.1371/journal.pone.0036768)